Proteomic Discovery of RNA-Protein Molecular Clamps Using a Thermal Shift Assay with ATP and RNA (TSAR)

Stanley I. Goldstein[1,2,3], Alice C. Fan[1,2], Zihao Wang[2], Sai K. Naineni[4], Johan Lengqvist[5], Alexey Chernobrovkin[5], Steve B. Garcia-Gutierrez[1], Regina Cencic[4], Kesha Patel[4], Sidong Huang[4], Lauren E. Brown[2], Andrew Emili[6], and John A. Porco, Jr.[1,2,*]

[1] BU Target Discovery Laboratory (BU-TDL), Boston University, Boston, MA, USA

[2] Department of Chemistry, Boston University, Boston, MA, USA

[3] Department of Pharmacology, Physiology, and Biophysics, Boston University, Boston, MA, USA

[4] Department of Biochemistry, McGill University, Montreal, QC, Canada

[5] Pelago Bioscience AB, Stockholm, Sweden

[6] Knight Cancer Institute, Oregon Health and Science University, Portland, OR, USA

* Correspondence: porco@bu.edu, stangold@bu.edu

Abstract

Uncompetitive inhibition is an effective strategy for suppressing dysregulated enzymes and their substrates, but discovery of suitable ligands depends on often-unavailable structural knowledge and serendipity. Hence, despite surging interest in mass spectrometry-based target identification, proteomic studies of substrate-dependent target engagement remain sparse. Herein, we describe the Thermal Shift Assay with ATP and RNA (TSAR) as a template for proteome-wide discovery of substrate-dependent ligand binding. Using proteomic thermal shift assays, we show that simple biochemical additives can facilitate detection of target engagement in native cell lysates. We apply our approach to rocaglates, a family of molecules that specifically clamp RNA to eukaryotic translation initiation factor 4A (eIF4A), DEAD-box helicase 3X (DDX3X), and potentially other members of the DEAD-box (DDX) family of RNA helicases. To identify unexpected interactions, we optimized a target class-specific thermal denaturation window and evaluated ATP analog and RNA probe dependencies for key rocaglate-DDX interactions. We report novel DDX targets of the rocaglate clamping spectrum, confirm that DDX3X is a common target of several widely studied analogs, and provide structural insights into divergent DDX3X affinities between synthetic rocaglates. We independently validate novel targets of high-profile rocaglates, including the clinical candidate Zotatifin (**eFT226**), using limited proteolysis-mass spectrometry and fluorescence polarization experiments. Taken together, our study provides a model for screening uncompetitive inhibitors using a systematic chemical-proteomics approach to uncover actionable DDX targets, clearing a path towards characterization of novel molecular clamps and associated RNA helicase targets.

Introduction

Rocaglates are a diverse family of natural products and synthetic congeners that have been subject to numerous synthetic and medicinal chemistry campaigns across academia and industry (1-12). Interest in their pharmacology was first stimulated by studies of crude *Aglaia* extracts showing anti-neoplastic potential in cellular and murine models of cancer (13). After the prototypical rocaglates rocaglamide (RocA) and silvestrol were found to drive this activity (14, 15), investigations in models of viral, protozoan, and bacterial infection broadened the utility of these compounds to include infectious disease applications (16-24). Our group and others have since expanded the rocaglate family to include hundreds of derivatives and novel subclasses, each with demonstrated activity across a range of disease models (3, 6, 12, 25); representative structures of natural and synthetic rocaglates used in this study are provided in **Figure 1**. Sustained interest in rocaglate drug discovery has culminated in the nomination of Zotatifin (**eFT226**) as a clinical candidate for both estrogen receptor-positive (ER+) breast cancer and SARS-CoV-2 infection (ClinicalTrials.gov identifiers: NCT04092673 and NCT04632381), further underscoring the tractability of the rocaglate family as broad-spectrum pharmaceutical agents.

The bulk of mechanistic studies converge on cap-dependent mRNA translation as a nexus for rocaglate bioactivity (26-30). Early experiments with naturally-derived rocaglates established these compounds as translation inhibitors that strengthen the association between mRNA transcripts and eukaryotic translation initiation factor 4A1 (eIF4A1) (31, 32), an abundant DEAD-box helicase (DDX) that unwinds secondary structure in mRNA transcripts destined for translation. This strengthened ternary association, hereby referred to as “clamping,” slows the dissociation of eIF4A1 from purine-rich 5’-UTRs, resulting in the steric blockade of ribosome recruitment (30). A crystallographic study by Iwasaki and coworkers revealed that rocaglates target a transient cleft formed between eIF4A1 and bound purine dinucleotides, thereby forming contacts with both biomolecules (33). It was subsequently shown by the Pelletier laboratory that rocaglates clamp eIF4A2, a close paralog of eIF4A1 also implicated in translation (25), and eIF4A3 (also known as DDX48), a protein involved in exon-junction complex (EJC) formation, although the consequences of eIF4A3 clamping have yet to be fully characterized (29). Finally, a study by Chen and coworkers used an unbiased mass spectrometry-based approach to identify DEAD-box helicase 3X (DDX3X) which like eIF4A1/2 is involved in translation initiation, albeit with a less well-defined role, as a low affinity target of RocA (28).

These four helicases share a highly conserved core domain common to at least 41 human DDX and 16 related DExH-box (DHX, hereafter binned with DDX for simplicity) helicases (HUGO Gene Nomenclature Committee) whose functions have been reviewed in detail (34, 35). Across the DDX family, the conserved core imparts ATP binding/hydrolysis and RNA binding activity, while variable N- and C-terminal domains differentiate DDX functions across diverse RNA-related processes such as translation, rRNA processing, and antiviral innate immunity (36-39). With such diverse roles, DDXs represent an attractive class of drug targets if they prove to be selectively ligandable. Thus, the understanding that eIF4A and DDX3X belong to a larger family of DDXs invites speculation as to whether synthetic rocaglates can be engineered to selectively target other DDX proteins. Conversely, undifferentiated targeting of eIF4A isoforms and DDX3X clouds distinctions between biological effects arising downstream of ligand binding (27-29). Target engagement becomes relevant in granular disease subtypes that may preferentially depend on certain helicases. As such, the identification of rocaglates selective for specific DDXs remains a key challenge.

The past decade of progress in mass spectrometry-based target deconvolution has enabled proteome-scale detection of target engagement in a single experiment (40). Proteomic thermal shift assays and related approaches (*e.g.* the mass spectrometry-based cellular thermal

shift assay (MS-CETSA) and the proteome integral solubility alteration assay, (PISA)) (41, 42) are now staples in the label-free target identification toolkit that are used at different stages of the drug discovery process to assist in target identification, medicinal chemistry optimization, ligand selectivity assessment, and validation of *in vivo* protein engagement (43-46). Despite widespread use, these assays suffer from drawbacks that hinder universal applicability. Live cell-based formats report on the downstream effects of compound treatment (*e.g.* changes in protein abundance) in addition to compound-induced thermal stabilization, which makes identification of direct protein targets more challenging (47). Lysate-based formats are useful in identifying direct targets but are performed under non-physiological conditions in which co-factors or co-substrates necessary for target engagement may become diluted or disrupted (43, 48).

To recapitulate intracellular binding dependencies, we reasoned that the addition of ATP and polypurine RNA required for rocaglate binding would promote target engagement in cell lysates. Here, we report a thermal shift method, termed the Thermal Shift Assay with ATP and RNA (TSAR), that allows for enhanced detection of rocaglate-induced clamping events. We show that ATP analogs and RNA substrates strongly promote formation of DDX-RNA rocaglate receptor complexes in cell lysates, a requisite for rocaglate binding. Conditions were optimized to detect rocaglate-induced stability changes to DDXs across a wide dynamic range. We show that TSAR is complementary to another lysate-based stability screen, limited proteolysis-mass spectrometry (LiP-MS). Structural docking-based analysis of DDX3X clamping by specific rocaglates serves as an example to guide structure-based design projects for five potential new additions to the rocaglate clamping spectrum. The workflows described herein can be applied to screen for multi-component interactions of other modalities and represent a new direction for stability proteomics as an evolving tool for drug discovery.

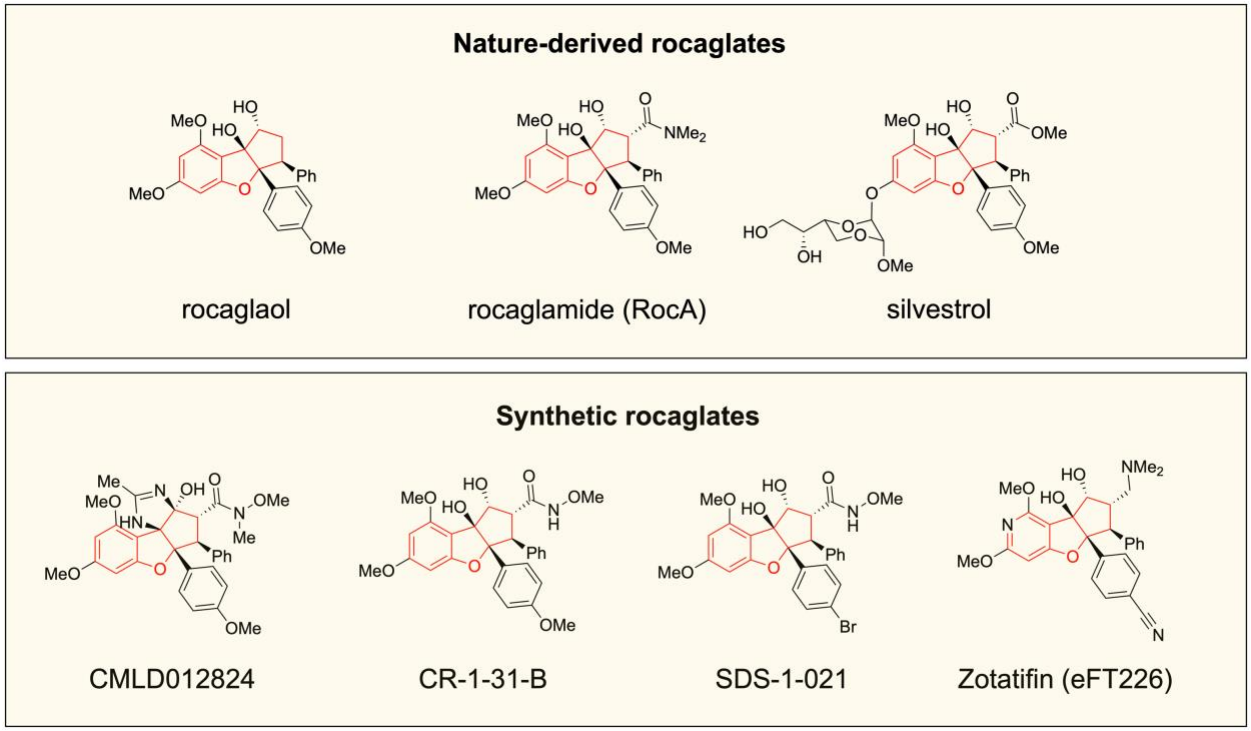

Figure 1. Rocaglates used in this study. Representative rocaglates with common cyclopenta[*b*]benzofuran core highlighted in red. Generated using ChemDraw (23.0.1).

Material and Methods

Cell culture

For live-cell PISA experiments, HEK293 or HepG2 cells (ATCC) were grown in Dulbecco's Modified Eagle Medium supplemented with 10% fetal bovine serum and 1X penicillin-streptomycin solution. When cells achieved ~90% confluency, cells were washed once with PBS, detached using TrypLE express, washed two more times with Hank's balanced salt solution (HBSS, Thermo Scientific) and pelleted again. Then cells were resuspended in the experimental buffer (20 mM HEPES, 138 mM NaCl, 1 mM $MgCl_2$, 5 mM KCl, 2 mM $CaCl_2$, pH 7.4) at a density of 40 MIO cells/mL which was used as the 2X cell suspension.

For lysate-based experiments, HEK293 and A549 cells (ATCC) were grown in Dulbecco's Modified Eagle Medium supplemented with 10% fetal bovine serum and 1X penicillin-streptomycin solution. When cells achieved ~90% confluency, cells were washed once with PBS, detached using TrypLE express, then washed 3X in HBSS. All remaining liquid was removed and cell pellets were flash frozen using liquid nitrogen and stored at -80 °C.

PISA assay in live cells

<u>PISA assay</u>

The 2X cell suspension and a 2X compound solution (6 *µ*M compound in experiment buffer with 2% DMSO) were combined in a 1:1 ratio. Then, each sample (3 *µ*M compound or 1% DMSO control) was incubated for 60 minutes at 37 °C with end-over-end rotation. For each cell type, each of the treated cell suspensions were divided into 48 aliquots (12 temperature points, four replicates) that were all subjected to a heat challenge for 3 minutes, each at a different temperature between 44 and 66 ºC. After heating, all temperature points for each test condition were repooled to generate individual integrated samples. Precipitated proteins were pelleted by centrifugation at 30,000*g* for 20 minutes and supernatants constituting the soluble protein fraction were collected. Then the total protein concentration of each soluble fraction was measured by Lowry DC Protein Assay (BioRad). From each soluble fraction, a volume containing a defined amount of total protein was taken for relative quantification using LC-MS/MS based isobaric labeling methodology as described below.

<u>Isobaric labeling and LC-MS/MS data collection</u>

Samples were subjected to reduction and denaturation with 5 mM *tris*(2-carboxyethyl)phosphine (TCEP) Bond-breaker (Thermo Scientific) followed by alkylation with 15 mM chloroacetamide. Proteins were digested with Lys-C (Wako Chemicals) and trypsin (1:40 ratio, Trypsin Gold, Promega). After complete digestion had been confirmed by nanoLC-MS/MS (<7% missed cleavage sites), samples were labeled with 16-plex Tandem Mass Tag reagents (TMTPro, Thermo Scientific) according to the manufacturer's protocol. Labeling reactions were quenched by addition of a primary amine buffer and the test concentrations and room temperature samples were combined into TMT16-plex sets. The labeled samples were subsequently acidified and desalted using a polymeric reversed phase sorbent (Oasis, Waters). LC-MS grade solvents and low-protein binding tubes were used throughout the purification. Samples were dried using a centrifugal evaporator. For each experiment, the dried labeled sample was dissolved in 20 mM ammonium hydroxide (pH 10.8) and subjected to reversed-phase high pH fractionation using an Agilent 1260 Bioinert HPLC system (Agilent Technologies) over a 1.0 x 150 mm C18 column (XBridge Peptide BEH C18, 300 Å, 3.5 µm particle size, Waters Corporation, Milford, USA). Peptide elution was monitored by UV absorbance at 215 nm and fractions were collected every

30 seconds into polypropylene plates. The 60 fractions covering the peptide elution range were evaporated to dryness, ready for LC-MS/MS analysis.

From the fractions collected, 30 pooled fractions were analyzed by high resolution nano LC-MS/MS on Q-Exactive HF-X Orbitrap mass spectrometers (Thermo Scientific) coupled to high performance nano-LC systems (Evosep One, Evosep, Denmark). MS/MS data was acquired using higher energy collisional dissociation (HCD) and full MS data was collected using a resolution of 120 K with an AGC target of 3e6 over the m/z range 375 to 1500. The top 15 most abundant precursors were isolated using a 1.4 Da isolation window and fragmented at a normalized collision energy value of 35. The MS/MS spectra (45K resolution) were allowed a maximal injection time of 120 ms with an AGC target of 1e5 to avoid coalescence. Dynamic exclusion duration was 30 s.

Protein identification and quantitative data extraction

Protein identification was performed by database search against 95,607 human protein sequences in Uniprot (UP000005640, download date: 2019-10-21) using the Sequest HT algorithm as implemented in the ProteomeDiscoverer 2.4 (PD2.4) software package. Data was re-calibrated using the recalibration function in PD2.4 and final search tolerance setting included a mass accuracy of 10 ppm and 50 mDa for precursor and fragment ions, respectively. A maximum of two missed cleavage sites was allowed using fully tryptic cleavage enzyme specificity (K, R, no P). Dynamic modifications were oxidation of Met, and deamidation of Asn and Gln. Dynamic modification of protein N-termini by acetylation was also allowed. Carbamidomethylation of Cys, TMTPro-modification of Lysine and peptide N-termini were set as static modifications.

For protein identification, validation was done at the peptide-spectrum-match (PSM) level using the following acceptance criteria: 1 % FDR determined by Percolator scoring based on Q-value, rank 1 peptides only. For quantification, a maximum co-isolation of 50% was allowed. Reporter ion integration was done at 20 ppm tolerance and the integration result was verified by manual inspection to ensure the tolerance setting was applicable. For individual spectra, an average reporter ion signal-to-noise of >20 was required. Further, shared peptide sequences were not used for quantification.

Thermal shift assay with ATP and RNA (TSAR) in cell lysates

Frozen cell pellets were lysed in ice-cold lysis buffer (20 mM HEPES, 138 mM NaCl, 5 mM KCl, 2 mM $MgCl_2$, 2 mM $CaCl_2$, cOmplete EDTA-free protease inhibitor, pH 7.4) via four successive freeze-thaw cycles using liquid nitrogen. Thawing was performed in a room temperature water bath until ~80% thawed, then completed on ice. After the final freeze-thaw cycle, lysates were clarified by centrifugation at 20,000 RCF and 4 °C for 15 minutes, then transferred to a new LoBind tube. Lysate was assayed using a Pierce BCA Protein Assay Kit and adjusted to 2.0 mg/mL (2X experimental concentration).

Depending on the experiment, different 2X buffer solutions were prepared by supplementing the lysis buffer with 2X concentrations of an ATP analog and/or RNA probe, both of which were first formulated as stock solutions in LC-MS grade water. Lysate was added 1:1 to the appropriate 2X buffer solution treated with the indicated test compound or DMSO (0.5% final concentration), gently mixed via pipette, and incubated at room temperature for 15 minutes. After incubation, the 1X lysate was distributed across a 96-well PCR plate (20 μL per well) and the plate was heated for 3 minutes in an Applied Biosystems ProFlex PCR System across a pre-defined temperature range consisting of six discrete heating temperatures. The six temperature points were equally spaced regardless of the temperature range used. Temperature ranges for individual experiments

are indicated in the Results section. After heating, the PCR plate was placed on ice and an equal volume of lysate (18 μL) was used to pool temperature points back to their original replicate samples. Protein aggregates were pelleted by centrifugation at 30,000 RCF and 4 °C for 30 minutes. 20 μL of supernatant (8 to 10 μg protein depending on heating temperatures) was transferred to new tubes containing 2 μL of Benzonase (~30 units) and incubated on ice for 30 minutes to digest nucleic acids. Finally, samples were mixed with 11 μL of 3X sample preparation buffer (600 mM HEPES pH 8.5, 1.5% SDS, 30 mM TCEP, 120 mM chloroacetamide) and heated to 95 °C for 10 minutes to denature, reduce, and alkylate proteins. Samples were processed using a single-pot solid phase-enhanced sample preparation method (SP3).

Limited proteolysis-mass spectrometry (LiP-MS) assay

Limited proteolysis was carried out with slight modification to the original protocol (49). Cell lysates were prepared as described in the TSAR methods section. A 2X experimental buffer solution containing AMP-PNP (2 mM) and $(AG)_8$ RNA (2 μM) was prepared in lysis buffer and spiked with the indicated test compound or DMSO (0.5% final concentration). Lysate and 2X buffer solution were mixed 1:1 and 55 μL of 1X lysate was aliquoted into each well of one 12-well row of a PCR plate. DMSO and test compound aliquots were alternated to account for variation across heating elements. At the same time, 5 μL of proteinase K solution (0.2 μg/μL in water) was aliquoted across one 12-well row of the same PCR plate. The PCR plate was placed inside an Applied Biosystems ProFlex PCR System and incubated for 5 minutes at 25 °C. At the 5-minute mark, 50 μL of lysate (50 μg of protein) was transferred to the row containing 5 μL of proteinase K using a 12-channel pipette. The proteinase K-lysate mixture was incubated for 4 minutes at 25 °C. At the 4-minute mark, the temperature program was automatically set to 99 °C and held for 10 minutes (with a 110 °C heated lid to limit evaporation) to inactivate proteinase K. After proteinase K inactivation, the samples were cooled to 4 °C and removed from the PCR system. To each sample, Benzonase solution was added (11 μL, ~30 units) and the samples were incubated on ice for 30 minutes to digest nucleic acids. Finally, a 33 μL aliquot of 3X sample preparation buffer (600 mM HEPES pH 8.5, 1.5% SDS, 30 mM TCEP, 120 mM chloroacetamide) was added to each sample, at which point the PCR plate was again heated for 10 minutes at 95 °C for 10 minutes to resolubilize aggregates and reduce and alkylate proteins. Care was taken to avoid contact between pipette tips and protein aggregates during introduction of sample preparation buffer. After cooling, a volume of 20 μL (~10 μg protein) was transferred to a new tube. Samples were processed using a single-pot solid phase-enhanced sample preparation method (SP3).

Sample preparation for TSAR and LiP-MS

Single-pot solid phase-enhanced sample preparation (SP3) was carried out with slight deviation to the previously described protocol (50, 51). Samples were mixed with ~100 μg of Sera-Mag carboxylate-modified magnetic beads (1:1, hydrophilic:hydrophobic beads) and proteins were precipitated using a 4X volume of acetonitrile. Samples were incubated on a ThermoMixer (24 °C, 1000 RPM) for 20 min, then centrifuged for 1 minute at 500 RCF, and beads drawn to a magnet for 2 minutes. Beads were washed on-magnet three times with 80% ethanol and once with 100% acetonitrile. Beads were air-dried, then resuspended in 50 μL of digestion buffer (100 mM HEPES pH 8.5, 1 mM $CaCl_2$, 0.01 μg/μL Trypsin/Lys-C mix). Proteins were digested on-bead in a ThermoMixer set to 37 °C for 18 hours with shaking. After digestion, samples containing beads were evaporated to dryness, resuspended in LC-MS grade water, then reacted with ~65 μg of isobaric tandem mass tag (TMTpro; ThermoFisher) multiplexing reagents (final reaction volume 20 μL, 30% acetonitrile) for 1 h. Samples were quenched with hydroxylamine, pooled,

and evaporated to dryness in a SpeedVac. The pooled sample was resuspended in 2% acetonitrile, acidified with formic acid, and desalted using a Pierce Peptide Desalting Spin Column (ThermoFisher). The eluate was again evaporated to dryness in a SpeedVac prior to high pH reversed-phase peptide fractionation.

High pH reversed-phase peptide fractionation for TSAR and LiP-MS

TMTpro-labeled peptides were fractionated using high pH reversed-phase chromatography on an Agilent 1260 Infinity Capillary LC equipped with an XBridge Peptide BEH C18 column (300Å, 3.5*µ*m, 1mm x 150mm, Waters Corporation). Peptides were resuspended in 2% acetonitrile and 0.1% NH_4OH, injected manually, and separated using a gradient of mobile phase A (2% acetonitrile, 0.1% NH_4OH in water) to mobile phase B (2% water, 0.1% NH_4OH in acetonitrile) at a flow rate of 75 *µ*L/min. Separation conditions were 100% mobile phase A for 5 minutes, a linear gradient to 12% mobile phase B for 5 minutes, a linear gradient to 32% mobile phase B for 35 minutes, a linear gradient to 45% mobile phase B for 8 minutes, a linear gradient to 70% mobile phase B for 1 minute, and a wash with 70% mobile phase B for 16 minutes (70 minutes total). Eluate fractions were collected from 20 to 68 minutes in 30 second time slices for a total of 96 fractions. Fractions were then concatenated into 24 pooled fractions and evaporated to dryness in a SpeedVac. For certain experiments, 12 non-adjacent pooled fractions were analyzed (52), while for others all 24 pooled fractions were analyzed (detailed in Experimental Design and Statistical Rationale section).

LC-MS/MS data acquisition and protein identification for TSAR and LiP-MS

Pooled fractions were resuspended in 2% acetonitrile, 0.1% formic acid in water at ~0.1 *µ*g/*µ*L and ~0.8 *µ*g of peptides were separated on an Easy-nLC 1200 system connected to an Orbitrap Eclipse mass spectrometer equipped with a FAIMS Pro Interface. Mobile phase A consisted of 2% acetonitrile, 0.1% formic acid in water and mobile phase B consisted of 0.1% formic acid in 80% acetonitrile. Peptides were first loaded onto an Acclaim PepMap C18 nano-trap column (100Å, 3*µ*m, 75*µ*m x 2cm, Thermo Scientific 164946) in mobile phase A, then separated on an EASY-Spray column (100Å, 2*µ*m, 75*µ*m x 500mm, Thermo Scientific ES903). Flow rate was set to 250 nL/min. Peptides were separated using a linear stepped gradient over either a 110 minute or 150 minute method. The mass spectrometer was operated in positive ion mode with a spray voltage of 2500V and a capillary temperature of 275 °C. Data dependent acquisition was perfomed in cycle time mode with three FAIMS compensation voltages (-35, -50, -65) and a cycle time of 1 second per compensation voltage. Precursor ion scans were acquired in the Orbitrap with a resolution of 60,000, a normalized AGC target of 100%, maximum injection time set to automatic (50 ms), and a scan range of 400-1600 m/z. Additional filters included MIPS mode set to peptide, a 60 second dynamic exclusion window, an intensity threshold of $2.5e^4$, and charge states of 2-6 for MS2. For MS2 scans, data were acquired in the Orbitrap with a resolution of 50,000, a normalized AGC target of 200%, maximum injection time set to automatic, and HCD collision energy set to 35%.

MS/MS raw files were split into separate CV-specific raw files, then searched using the Andromeda search engine in MaxQuant software (version 2.0.3.0) (53) against the Uniprot Human reference proteome (downloaded February 8, 2023; 20,594 sequences) and the MaxQuant contaminants database. Searches were performed using default MaxQuant settings with minor modification. Briefly, reporter ion MS2 mode was used with internal and terminal TMTpro 16plex labels corrected for isotopic impurities according to manufacturer-supplied correction values. Searches allowed for methionine oxidation and N-terminal protein acetylation

as variable modifications, while cysteine carbamidomethylation was set as a fixed modification. Enzyme specificity was set to Trypsin/P with a maximum of two missed cleavages allowed. Precursor ions were searched with a mass tolerance set to 4.5 ppm and fragment ions were searched with a mass tolerance set to 20 ppm. Peptide spectrum match and protein FDRs were set to 0.01 using a target-decoy database search strategy (54). The minimum score for modified peptides was 40. Only unique peptides were used for quantification.

Proteomics data analysis

Additional data filtering and statistical analyses were conducted in R: A language and environment for Statistical Computing (R Foundation for Statistical Computing, http://www.R-project.org) using the Omics Notebook analysis pipeline (55), which performs differential analysis using the limma R package (56). The MaxQuant output file designated “proteinGroups” provided a table of corrected reporter ion intensities that, after removal of contaminants, reverse hits, and proteins identified based on modified peptides, was log transformed and normalized (detailed in Experimental Design and Statistical Rationale Section). Group comparisons were conducted using moderated t-tests with a Benjamini-Hochberg correction to contain the false discovery rate at 1 or 5% depending on the experiment. Only proteins that were quantified with at least 2 unique peptides were included in protein level analyses. Volcano plots, scatterplots, and heat maps were built using the R package ggplot2 or generated in GraphPad Prism (9.3.1). Hits were filtered as described in the Experimental Design and Statistical Rationale section.

Purification of recombinant proteins

pET15b-His6-eIF4A1, pET15b-His6-eIF4A3, pColdII-His6-DDX3X, pET21a-His6-DDX21, or pColdII-His6-DDX50, were transformed into BL21 (DE3) codon+ *Escherichia coli* cells and cultured at 37 °C until the OD600 reached 0.6. Bacteria were induced with 1 mM IPTG and growth of cultures containing pET-backbone plasmids was continued for 3 h at 37 °C, while pColdII plasmid containing cultures were shifted to grow at 16 °C for 24h. Recombinant His6-eIF4A1, His6-eIF4A3, His6-DDX3X, His6-DDX21, and His6-DDX50 proteins were purified on a Ni^{2+}-NTA agarose column followed by purification on a Q-Sepharose fast-flow matrix and elution with a linear salt gradient (100 to 500 mM KCl). Fractions containing protein were dialyzed against Buffer A (20 mM Tris-HCl [pH7.5], 10% glycerol, 0.1 mM ethylenediaminetetraacetic acid (EDTA)) overnight at 4 °C, and stored in aliquots at −80 °C.

Fluorescence polarization assays

1.5 μM recombinant eIF4A1, eIF4A3, DDX3X, DDX21, or DDX50 protein was added to 10 nM FAM labeled poly $(AG)_8$-RNA in binding buffer (14.4 mM HEPES-KOH [pH 8], 108 mM NaCl, 1 mM MgCl2, 14.4% glycerol, 0.1% DMSO, and 2 mM DTT) and 1 mM ATP in the presence or absence of the indicated compound. Following assembly, binding reactions were incubated for 10 min at room temperature (RT) in the dark, after which polarization values were determined using a Pherastar FS microplate reader (BMG Labtech). Data was analyzed using GraphPad Prism (9.3.1).

Computational modeling

Ligand Preparation

Schrödinger's LigPrep in the Maestro software environment (Version 2023-1, Build 128) was employed to prepare two compounds (Zotatifin and **CR-1-31-B**) for docking studies. During ligand preparation, possible protonation states prediction of the compounds was performed using Epik in the pH range of 7.4 +/- 2.0. For Zotatifin, LigPrep produced two predicted states for docking: the neutral species, and a protonated state where the dimethylamino nitrogen is positively charged. For the rocaglate **CR-1-31-B**, Epik produced only neutral species.

Rigid Receptor Docking

Glide docking was performed in Schrödinger's Maestro software environment (Version 2023-1, Build 128). PDB X-ray structure 5ZC9 was prepared for use as the docking receptor through the default Protein Preparation Workflow, involving structure pre-processing, hydrogen-bond optimization, restrained minimization (S-OPLS force field, hydrogen atoms freely minimized and heavy atoms minimized to r.m.s.d. 0.3), and removal of water >4 Å from heteroatoms. For each compound, the highest-scored docking pose exhibiting the "canonical" rocaglate positioning observed in the 5ZC9 structure was selected for analysis.

Induced Fit Docking

Induced Fit Docking (IFD) was performed in Schrödinger's Maestro software environment (Version 2023-1, Build 128). PDB X-ray structure 7LIU was prepared for use as the docking receptor through the default Protein Preparation Workflow as described above. To define the binding site, the center-of-mass of each docked ligand was restrained to a 10 Å box positioned at the centroid of the following residues: Val328, Glu332, Gln360, Arg363 (from DDX3X), C704 and G705 (from the DNA-RNA hybrid oligonucleotide). During IFD, all protein side chains within 5 Å of the docked ligand were designated flexible, while all oligonucleotide side chains were designated as rigid. For each ligand, 11-18 ranked IFD poses were produced. For each compound, the highest-scored IFD pose exhibiting the "canonical" rocaglate positioning observed in the 5ZC9 structure was selected for analysis.

Experimental Design and Statistical Rationale

For all proteomics data sets, group comparisons were performed using a moderated t-test to account for noise in variance estimates. P values were adjusted using the Benjamini-Hochberg method to contain false discovery rates at the levels specified below.

The two live cell PISA experiments corresponding to Figure 2 were performed with four biological replicates per treatment group (test compound or DMSO control), which we have found to sufficiently power statistical analyses. A total of 30 high pH fractions were analyzed by LC-MS/MS for each experiment. Log-transformed reporter intensity values were normalized using locally estimated scatterplot smoothing (LOESS). For significance, no fold change cutoff was applied, but a stringent adjusted p value of .01 was used. Each of these two 16plex experiments involved other compounds that were outside the scope of this study and thus were not reported in the manuscript.

Lysate-based TSAR method development experiments corresponding to Figures 3 through 6 were performed using duplicates to maximize the number of experimental groups allowable in a single isobaric labeling experiment (*i.e.* 8 groups per 16plex). We note that experiments run with technical duplicates are underpowered for target identification. For these experiments, we

focused on fold-change responses for known rocaglate targets, statistically significant hits, and high probability speculative targets (*e.g.* DDX21). Speculative targets of interest were followed up later in the manuscript with sufficiently powered experiments. A total of 12 high pH fractions were analyzed by LC-MS/MS for each of these experiments. Lysate-based TSAR profiling experiments corresponding to Figure 7 were performed using quadruplicates. A total of 24 high pH fractions were analyzed by LC-MS/MS for each of these experiments. All lysate-based TSAR experiments were performed using a 16plex design, except the RNA concentration dependence experiment (corresponding to Figure 6B) which was performed using an 18plex design. Log-transformed reporter intensity values were median normalized. Significance thresholds were $|\log_2 FC| > 0.2$ and an adjusted p value of .05.

Limited proteolysis-mass spectrometry (LiP-MS) experiments are extremely sensitive to small differences in proteolysis incubation times. In our hands, even a ~10 second delay leads to significantly altered proteolytic cleavage patterns. To streamline the workflow and avoid differences in incubation times, we used a 12-channel pipette to mix lysate with proteinase K across one row of a PCR plate simultaneously, allowing the remainder of the procedure to be completed using a thermal cycler program. Therefore, LiP-MS experiments were performed with six replicates per condition for a total of 12 samples per isobaric labeling experiment. A total of 24 high pH fractions were analyzed by LC-MS/MS to maximize tryptic peptide identifications. Log-transformed reporter intensities were quantile normalized. For significance, no fold change cutoff was applied, but a stringent adjusted p value of .01 was used.

Results

Rocaglate-induced network effects confound live-cell thermal shift assays

In past work, we followed rocaglate synthesis campaigns with *in vitro* fluorescence polarization (FP) assays with isolated recombinant enzyme to measure RNA clamping across eIF4A isoforms (25, 29). While FP enabled comparisons of eIF4A affinity within our rocaglate collection, the method has some drawbacks: it requires time-consuming protein production, optimization, and the use of non-native protein. Most importantly, this assay does not address the possibility of unintended off-targets.

Given our goal of identifying novel interactions with DEAD/DExH-box (DDX) helicases, we initially set out to profile rocaglates using live-cell PISA, a higher-throughput version of the mass spectrometry-based cellular thermal shift assay (MS-CETSA) which reports on compound-induced thermal stability changes of proteins in a cellular context (41, 42). To benchmark assay performance, we tested the well-characterized synthetic rocaglate **CR-1-31-B** (**Figure 1**), a confirmed binding partner of all eIF4A isoforms with demonstrated biological activity (2). HepG2 and HEK293 cells were treated with **CR-1-31-B** (3 μM), distributed across a PCR plate, subjected to a heat challenge, repooled, and proteomes processed using an isobaric labeling workflow. We observed weak but statistically significant eIF4A1 stabilization in HepG2 cells, although no effect was seen for eIF4A2 or eIF4A3 (**Figure 2A**). A study by Chen and coworkers reported DDX3X as a low affinity target of RocA (28). Indeed, we found DDX3X was also stabilized by **CR-1-31-B** in HepG2 cells. Conversely, a close paralog, DDX3Y, a speculative rocaglate target, did not reach statistically significant stabilization. Rather, the helicases DHX9 and DHX29 were among the most significantly altered proteins, suggesting either direct targeting or a network-driven interaction. In contrast to HepG2 cells, results from HEK293 cells did not recapitulate any known rocaglate targets (**Figure 2B**), possibly due to a lack of target saturation, although DDX21 was destabilized. While there was a moderate correlation in differentially altered proteins between cell lines (**Figures 2C-D**), the incomplete target profiling pointed to the limitations of the live cell format.

On the other hand, there was evidence of perturbation at the network level. We used STRING-DB (57) to re-construct functional networks with significantly altered proteins, clustered the results, and determined functional enrichments among the largest groupings (**Figure S1**). Strikingly, in both cell lines, proteins involved in translation (eEFSEC, eIF3 complex members, eIF4G1/2, PABPC1, PAIP1/2, SRP9/14 and others) were altered by ligand treatment (**Figures 2D** and **S1A-B**). Given that rocaglates sequester eIF4A1/2 away from active eIF4F (26), altered stability of these proteins likely reflects disruption of 48S translation initiation complex assembly. Differential stabilization of DHX9 and DHX29 (**Figure 2A**), which also resolve mRNA secondary structures, may be a consequence of increased reliance on these and potentially other helicases in response to terminal clamping of eIF4A1/2 and DDX3X (58). Targeting of eIF4A3, an eIF4A isozyme involved in splicing, was evident by ligand induced destabilization of MAGOH, a member of the exon junction complex, and splicing factors such as SLU7 and SRSF3. Intriguingly, our network analysis showed alterations to clusters enriched for ribosome biogenesis (**Figure S1A**) and rRNA processing (**Figure S1B**), annotations assigned to DDX21, although broad alterations of RNA binding proteins we observed confounded interpretation (59).

In summary, our data show that live-cell PISA can be useful to study pathway interactions but falls short for the unambiguous assignment of direct rocaglate targets. We therefore opted to measure thermal stabilization in cell lysate to allow for improved detection of direct ligand-protein engagement while muting network effects (47).

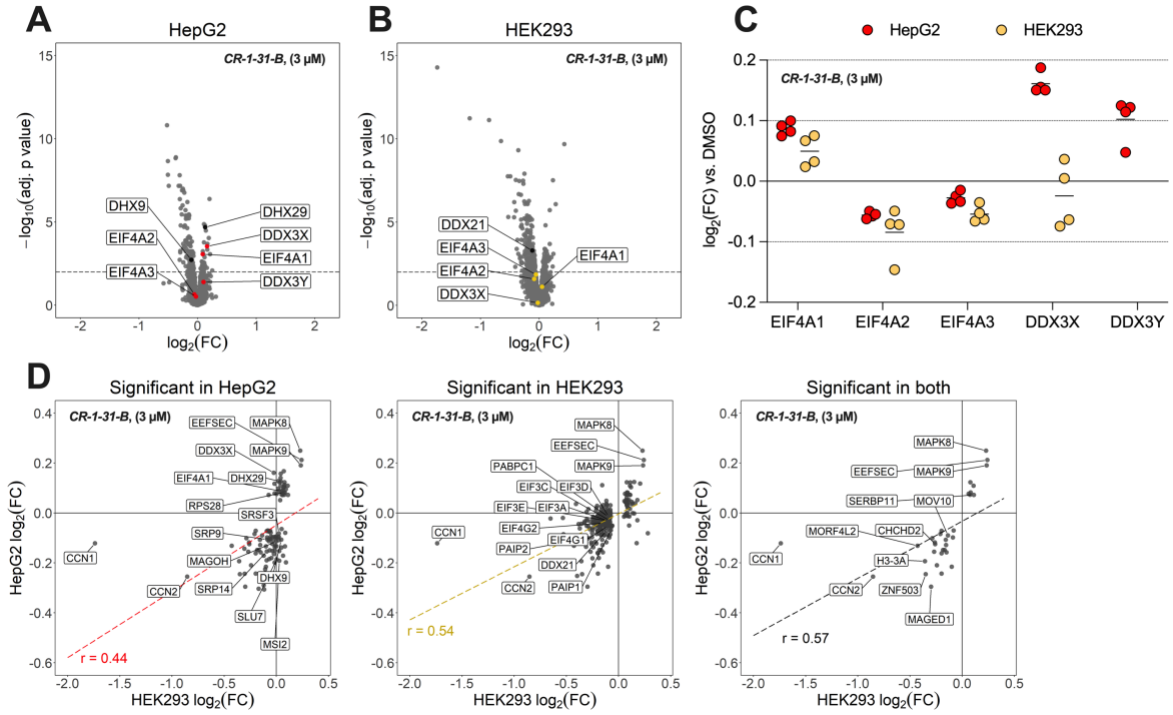

Figure 2. **Proteome integral solubility alteration (PISA) assay with CR-1-31-B in live cells.** Live cells were treated with **CR-1-31-B** (3 *μ*M) or DMSO (n = 4) and assayed *via* PISA. Volcano plots depict differentially stabilized proteins in HepG2 (**A**) and HEK293 (**B**) cell lines with known DDX protein targets colored red (HepG2) or yellow (HEK293) and other significant DDX/DHX RNA helicases colored black and labeled. The x-axis indicates log-fold change in protein abundance in compound-treated cells. Statistical significance was determined using a moderated t-test followed by Benjamini-Hochberg correction (adj. p value ≤ .01, indicated by the dashed horizontal line). **(C)** Log-fold change values for known DEAD-box protein targets and the

speculative target DDX3Y extracted from live cell PISA data. **(D)** Correlation plots of log-fold change values for all proteins that were significantly altered in HepG2, HEK293, or both cell lines. A best fit line was drawn through each data set.

Thermal stabilization of pre-formed rocaglate receptors

DDX enzymes undergo repetitive cycles of RNA unwinding and release coupled to ATP hydrolysis and ADP release (60). While studies from Iwasaki and coworkers show that rocaglate-induced DDX clamping is ATP-independent (30), ATP is known to increase DDX affinity for RNA substrates (61) and therefore promotes the formation of rocaglate-competent DDX-RNA complexes, or rocaglate receptors (**Figure 3A**). Iwasaki and coworkers also showed that RocA engages eIF4A1:RNA complexes in the presence of ATP analogs that mimic each step of the hydrolytic cycle, including the post-ADP release state (30). However, the strongest interaction occurs in the ATPase ground state mimicked using the non-hydrolysable ATP analog AMP-PNP. Finally, crystallographic data supports the requirement for polypurine RNA in the rocaglate binding site of eIF4A1 (33); Chen and coworkers use a covalent RocA probe and *in vitro* FP assays to show that this purine specificity extends to DDX3X (28). Informed by this body of knowledge, we used lysate to probe the effects of additives that enable RNA clamping *in vitro* (16, 25, 28-30).

Accordingly, we tested whether a saturating concentration of **CR-1-31-B** (30 μM) could thermally stabilize rocaglate targets in HEK293 cell lysate pre-incubated with polypurine $(AG)_8$ RNA (1 μM), the non-hydrolysable ATP analog AMP-PNP (1 mM), both additives, or neither (control). Lysate samples were then incubated with test compound or DMSO, heated across a range of temperatures (44 – 64 °C), and repooled before processing for LC/MS analysis.

We found that while neither additive alone enabled the stabilization of known DDX targets, together they led to significant **CR-1-31-B**-induced stabilization of eIF4A1, eIF4A3, and DDX3X (**Figures 3B-C** and **S2**). We also observed a trend toward stabilization for eIF4A2 and DDX21, though they did not reach statistical significance with only two replicates per condition. DHX9 and DHX29, which were significantly altered in live-cell PISA, showed no indication of direct engagement, while mitochondrial processing peptidase subunit alpha (PMPCA) was a new hit in all conditions (**Figure S2A-D**), suggesting RNA-independent binding.

To better understand the interplay between thermal stabilization and additive helicase co-substrates, we extracted abundance measurements for each DDX from the global data (**Figure 3C**). Compared to the control condition, most DDXs did not respond to RNA alone, but a subset formed highly stabilized complexes with $(AG)_8$ RNA in the presence of AMP-PNP independent of **CR-1-31-B** (*e.g.* DDX5, DDX17). For this subset, high $(AG)_8$ RNA-induced stabilization may leave little room for additional overall stabilization upon rocaglate binding, urging careful consideration for assay design and data interpretation. In some cases, AMP-PNP alone was sufficient for stabilization (*e.g.* DDX21, DDX50), with little or no contribution from additive RNA – such proteins may prefer to bind endogenous RNA. In a select few cases (DDX42, DHX16, and DHX29), we observed destabilization, indicating that decreased stability can be indicative of DDX-RNA engagement.

For most helicases, however, there was no statistically significant change across any pair of conditions in the absence of **CR-1-31-B**. Critically, we note that AMP-PNP and $(AG)_8$ RNA (alone or together) did not alter eIF4A isoforms or DDX3X in the absence of **CR-1-31-B**, suggesting that the absence of stabilization by additives does not preclude subsequent stabilization by a rocaglate. Taken together, these results support a requirement for an ATP analog and exogenous RNA to promote the formation of stable rocaglate receptors in our Thermal Shift Assay with ATP and RNA (TSAR).

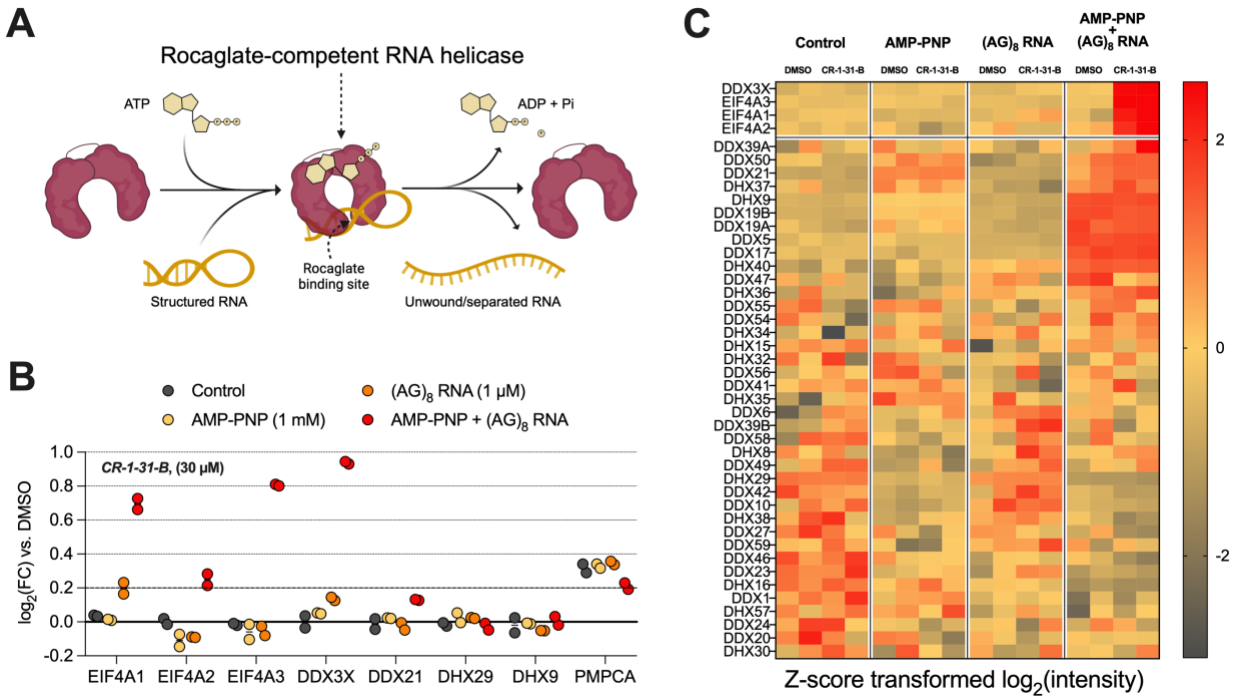

Figure 3. **Additive helicase co-substrates promote thermal stabilization of rocaglate targets. (A)** Schematic of ATP-dependent RNA binding by a DEAD-box helicase (made using BioRender.com). ATP and RNA binding are coupled, as are ATP hydrolysis and RNA release. **(B)** HEK-293 cell lysates were pre-loaded with AMP-PNP (1 mM), $(AG)_8$ RNA (1 μM), both, or neither and treated with **CR-1-31-B** (30 μM) or DMSO (n = 2), then assayed for **CR-1-31-B**-induced thermal stabilization. Extracted log-fold change values are shown for selected proteins. The dashed line indicates the fold-change threshold ($|\log_2 FC| > 0.2$). **(C)** Heat map of Z-score transformed log-intensity values for all DDX/DHX protein detected in the experiment (no significance threshold applied). Known DDX targets are separated at the top. Rows were clustered by average Euclidean distance.

Target class-specific temperature selection

Encouraged by our results, we next worked to improve TSAR assay functionality. We looked to the work of Li and coworkers who showed that appropriate temperature selection can improve the sensitivity of PISA readouts by magnifying stabilization fold-change values for proteins with melting points in a temperature range of interest (62). To inform temperature selection, we obtained thermal stability data from the Meltome Atlas (63), a publicly available dataset that provides cell line- and species-specific protein melting curves "across the tree of life." From the A549 cell lysate meltome, we extracted melting points for all available DDX proteins which spanned a temperature range of ~46 to ~64 °C (**Figure 4A**). These temperatures formed the lower and upper brackets of our experimental temperature ranges, of which four (46, 48, 50, and 52 to 64 °C) were selected for testing in two different experiments.

In the first experiment, we added **CR-1-31-B** (30 μM) to A549 cell lysate pre-loaded with AMP-PNP (1 mM) and $(AG)_8$ RNA (1 μM) to evaluate stability shifts of bona-fide rocaglate targets. Each of the four temperature ranges was tested using technical duplicates for a total of 16 samples that were processed in one TMTpro experiment. Switching to a male-derived A549 lysate afforded us the chance to screen for engagement of DDX3Y, a paralog encoded in the Y-

chromosome. As expected, raising the lower end of the temperature bracket boosted sensitivity for eIF4A and DDX3X binding with each successive shift upward (**Figure 4B**). Conversely, DDX3Y was stabilized but showed only marginal increases in log-fold change between the lowest and highest ranges. Notably, the log-fold change response of eIF4A2, which displays diminished sensitivity due to high thermal stability (**Figure 4A**), nearly doubled across conditions.

For the next experiment, we focused on improving sensitivity for stability shifts of other DDXs. To choose a test ligand in the absence of rocaglates known to target other DDXs, we reasoned that the lack of nucleotide specificity within the helicase core, which interacts solely with the RNA sugar-phosphate backbone, renders most RNA molecules suitable surrogates (34). Therefore, we induced stability shifts using an excess of $(AG)_8$ RNA (10 μM) and AMP-PNP (5 mM), which we expected to engage most DDXs. In this scenario, we observed 30 helicases with a significant change in stabilization in at least one of the four tested temperature ranges. This time, the benefit of increasing temperature reached a plateau, and a bottom bracket of 50 °C proved optimal for the detected helicases (**Figure 4C**). We therefore selected 50 to 64 °C as a working temperature range and moved on to evaluate and optimize other assay conditions.

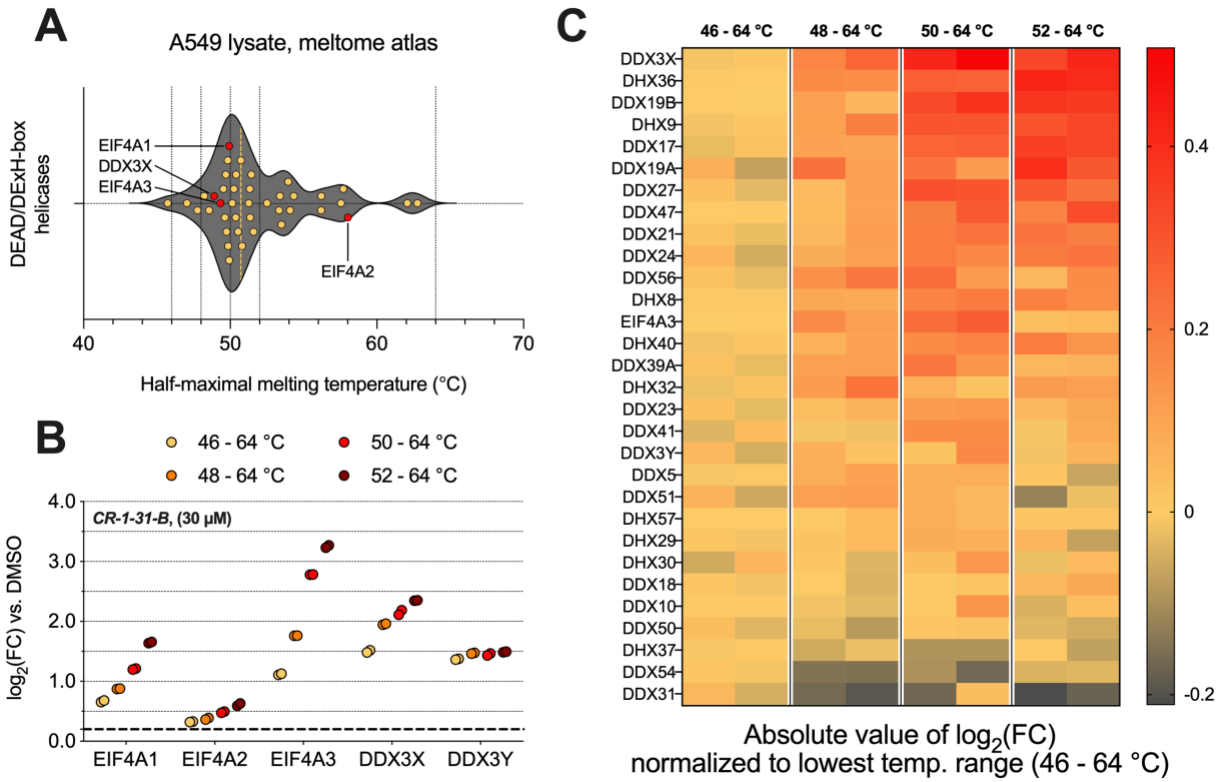

Figure 4. **Evaluation of heating temperatures to increase sensitivity. (A)** Distribution of DDX/DHX protein T_m values in A549 cell lysate extracted from Meltome Atlas. **(B)** Extracted log-fold change values for known DDX/DHX targets of **CR-1-31-B** (30 μM) in A549 lysate tested at four heating temperature ranges (n = 2). The dashed line indicates the significance threshold ($|\log_2 FC| > 0.2$). **(C)** Temperature-dependent incremental changes in sensitivity to stability shifts induced by AMP-PNP + $(AG)_8$ RNA. Absolute values of fold-changes were normalized to those of the lowest temperature range which was set to zero. Positive and negative values therefore represent increased and decreased sensitivity, respectively. Only helicases significantly altered ($|\log_2 FC| > 0.2$ and adj. p value ≤ .05) in ≥ 1 temperature range were included. Rows were ordered by rank sum of $|\log_2 FC|$.

Evaluation of ATP analogs

Given the importance of using an ATP analog in forming rocaglate receptors, we compared AMP-PNP to another non-hydrolysable ground state analog, AMP-PCP, along with ATP (1 mM each) to determine how these additives influence clamping in A549 lysate pre-loaded with $(AG)_8$ RNA (1 μM). As a test case we evaluated a different compound, the amidino-rocaglate (ADR) **CMLD012824** (10 μM) (**Figure 1**), one of the most potent translation-inhibiting rocaglates reported to date (25).

Across eIF4A and DDX3 isoforms, **CMLD012824**-induced thermal stabilization was greatest with AMP-PNP and moderate with AMP-PCP (**Figures 5A-E**). Interestingly, while ATP alone appeared to engage the broadest range of DDXs (**Figure 5F**), it resulted in the weakest clamping across DDX targets with the exception of eIF4A1. We also detected stabilization of DDX21 using AMP-PNP. Across all conditions, we again detected comparable stabilization of PMPCA, but differential stabilization of nucleic acid binding proteins such as ISY1, XPO7, and ZNF428. These differences may reflect alteration of ATP-dependent RNA binding protein interactomes. Based on enhanced assay sensitivity, we opted to use AMP-PNP in TSAR screens moving forward.

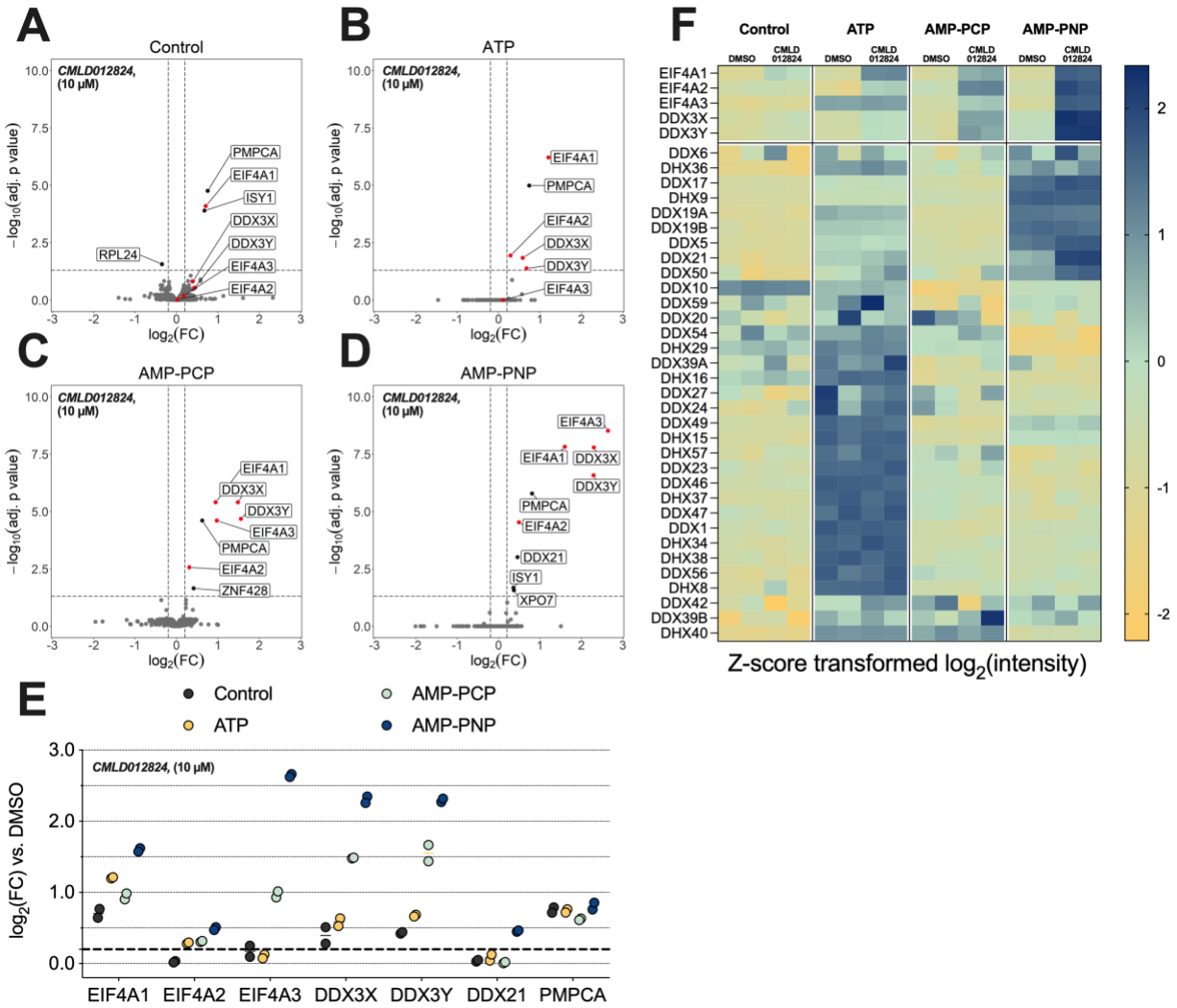

Figure 5. **Comparison of CMLD012824-induced stability shifts using ATP analogs.** A549 cell

lysate was pre-loaded with $(AG)_8$ RNA (1 μM) and water (control) **(A)**, ATP **(B)**, AMP-PCP **(C)**, or AMP-PNP **(D)** (1 mM each) then treated with **CMLD012824** (10 μM) or DMSO (n = 2) and assayed for **CMLD012824**-induced thermal stabilization. The volcano plot depicts differentially stabilized proteins, with DDX protein targets colored red. The x-axis indicates log-fold change in protein abundance in compound-treated samples. The dashed lines indicate significance thresholds ($|\log_2 FC| > 0.2$ and adj. p value ≤ .05). **(E)** Extracted log-fold change values for selected thermally stabilized proteins. The dashed line indicates the significance threshold ($|\log_2 FC| > 0.2$). **(F)** Heat map of Z-score transformed log-intensity values for all DDX/DHX proteins detected in the experiment (no significance threshold applied for inclusion).

Comparison of RNA additive parameters

The polypurine RNA requirement is a key feature of the rocaglate-DDX binding mechanism. To evaluate the significance of RNA base composition using TSAR, we compared **CR-1-31-B** (30 μM) target stabilization in A549 lysate across a panel of RNA probes (1 μM each): $(AG)_5$ (purine 10mer), $(AG)_8$ (purine 16mer), $(AU)_8$ (mixed 16mer), and $(CU)_8$ (pyrimidine 16mer).

Predictably, all eIF4A and DDX3 isoforms showed a strong preference for polypurine RNA, with the purine 16mer yielding the greatest fold-change values across targets (**Figure 6A**). We observed weak (not significant) destabilization of eIF4A1 and eIF4A2 in the presence of mixed and pyrimidine RNA. Conversely, DDX3X and DDX3Y were weakly stabilized in the presence of mixed and pyrimidine RNA. Having confirmed that polypurine RNA is a suitable and specific substrate for TSAR studies, we next asked how additive RNA concentration can influence TSAR readouts.

In theory, ATP, RNA, and rocaglate contribute sequentially to the overall fold-change in DDX thermal stability. First, ATP binding promotes RNA binding, resulting in a primary stability shift relative to unliganded DDX; next, a rocaglate binds in the helicase core and induces a secondary stability shift. Our TSAR assay necessarily reports the fold-change of this secondary interaction and may rely on relatively weak primary stabilization for sensitivity to rocaglate engagement. We thus reasoned that too much additive RNA could prematurely saturate DDX targets, resulting in a relatively small rocaglate-induced thermal shift. If true, DDXs with high intrinsic affinity for an RNA probe would appear less stabilized under saturating RNA concentrations, potentially dampening rocaglate-driven fold-change and masking real target engagement. To test this hypothesis in A549 lysates, we measured overall stabilization fold-change across a range of $(AG)_8$ RNA concentrations (0.3 to 30 μM) with a fixed **CMLD012824** concentration (10 μM). Our design included RNA-negative controls for determination of primary and overall fold-change and **CMLD012824**-negative 0.3 μM and 30 μM RNA controls for determination of secondary fold-change. Due to the replicate limitations of a TMTpro design, we compared secondary fold-change at 0.3 μM and 30 μM RNA to that of 1 μM RNA in the ATP analog experiment (extracted from **Figure 5E**).

As expected, overall stabilization of eIF4A and DDX3 was saturable with increasing RNA concentration in the presence of a fixed amount of **CMLD012824** (**Figure 6B**). At $(AG)_8$-RNA concentrations above 1 μM, overall stabilization of these targets plateaued, implying no added benefit from increasing RNA concentration. On the other hand, we saw differences in **CMLD012824**-induced stabilization between 0.3, 1, and 30 μM $(AG)_8$ RNA (**Figure 6C**). At high RNA concentration (30 μM), rocaglate-induced DDX3X stabilization diminishes to a value below that of moderate and low RNA concentration (1 and 0.3 μM). For DDX21, 1 μM RNA appears optimal among the concentrations tested. On the other hand, compound-induced stabilization of eIF4A isoforms is substantially weaker at low RNA concentration, but comparable at moderate

and high concentrations. These divergences likely stem from differential DDX occupancy by RNA prior to rocaglate engagement. The notion that intrinsic affinity for an RNA probe affects rocaglate-induced thermal stabilization is further supported by **Figure 6B**, which shows high stabilization of DDX3X by 30 μM RNA alone with comparably weak stabilization of eIF4A. Taken together, these results confirm that a simple polypurine probe at a 1 μM concentration is suitable for rocaglate clamping studies using TSAR.

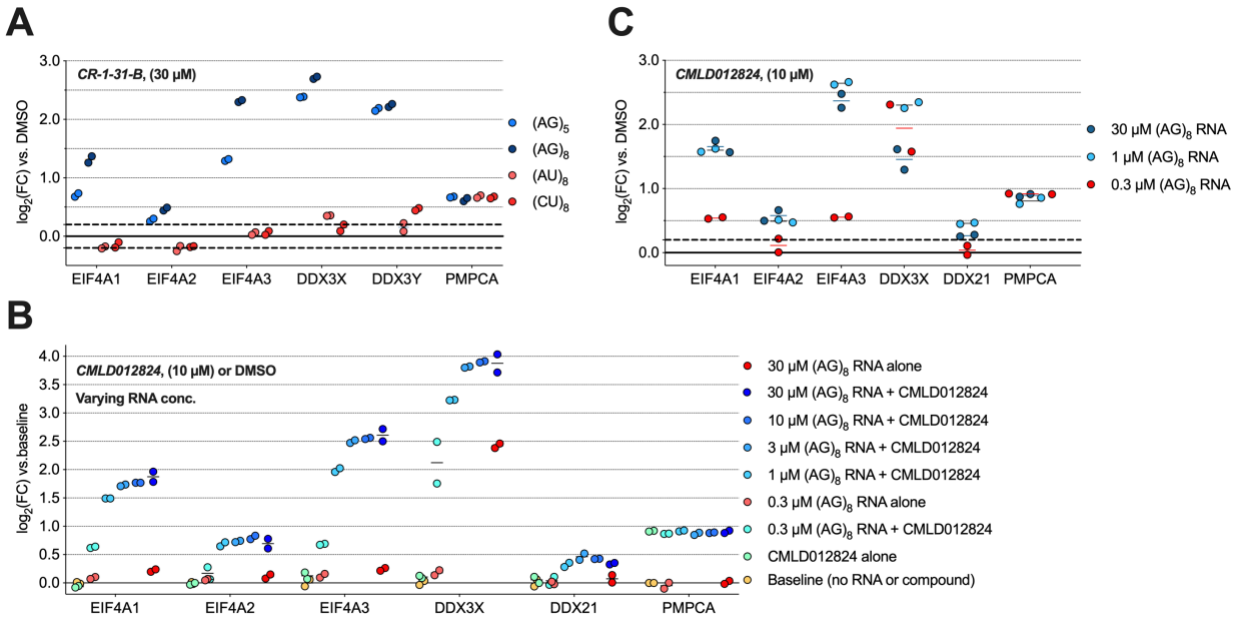

Figure 6. **Evaluation of additive RNA. (A)** A549 cell lysate was pre-loaded with AMP-PNP (1 mM) and one of four different single stranded RNA probes (1 μM), then treated with **CR-1-31-B** (30 μM) or DMSO (n = 2) and assayed. The plot depicts extracted log-fold changes for selected stabilized proteins. The dashed line indicates the significance threshold ($|\log_2 FC| > 0.2$). **(B)** A549 cell lysate was pre-loaded with AMP-PNP (1 mM), increasing concentrations of $(AG)_8$ RNA, and **CMLD012824** (10 μM) or DMSO (n = 2) and assayed for thermal stabilization. The plots depict extracted fold-change in protein abundance (stabilization) values relative to an RNA- and compound-naïve negative control (labeled "Baseline"). **(C)** Extracted fold-change values for DDX proteins stabilized by **CMLD012824** derived from two separate experiments. Results for the 0.3 and 30 μM RNA experiment are drawn from **Figure 6B**. Results for the 1 μM RNA experiment are drawn from **Figure 5D**. Both experiments were run using the same batch of cell lysate. Colored lines indicate mean fold-change for the given set of conditions. The dashed line indicates the significance threshold ($|\log_2 FC| > 0.2$).

TSAR profiling of the rocaglate target spectrum

Having gained an understanding of optimal TSAR assay parameters, we forged ahead and evaluated a diverse set of representative rocaglates with varied core functionality. Our panel consisted of rocaglaol, RocA, silvestrol, **CR-1-31-B**, **SDS-1-021** (64, 65), and the clinical candidate Zotatifin (**eFT226**) (**Figure 1**). Each compound was tested at a concentration of 10 μM in A549 cell lysate pre-loaded with AMP-PNP (1 mM) and $(AG)_8$ RNA or $(CU)_8$ RNA (1 μM), totaling four separate experiments with each rocaglate-RNA pair tested in quadruplicate. We used the same batch of lysate across all four experiments to allow for head-to-head comparisons of fold-

change (*i.e.* relative affinity). Full TSAR profiles represented as volcano plots are provided in **Figures 7A** (polypurine RNA) and **S3A** (polypyrimidine RNA).

As anticipated, in the presence of polypurine RNA, all rocaglates stabilized eIF4A1, eIF4A2, and, in line with the recent report from Naineni and coworkers, eIF4A3. Since DDX3X was reported as a target of RocA, it has been unclear whether DDX3X is a target of any other rocaglates. Indeed, we found that each compound tested stabilized not only DDX3X but its close paralog DDX3Y. We note the broad dynamic range observed for stabilization of eIF4A1, eIF4A3, and DDX3 isoforms, which should allow for comparison of relative affinities. Indeed, Zotatifin, touted for its eIF4A-selectivity, produced the smallest shift in DDX3 stabilization among the compounds tested (**Figure 7B**). In agreement with results in **Figure 6A,** there was little notable eIF4A or DDX3 clamping when using a polypyrimidine probe; the lone exception was for **SDS-1-021**, which mildly stabilized DDX3X and weakly (below the fold-change cutoff) destabilized eIF4A1 and eIF4A2 (**Figure S3A-B**).

Rocaglate-induced clamping of eIF4A and DDX3X is well understood, but whether rocaglates can similarly engage other members of the DDX family has remained an open question. Remarkably, using a polypurine probe, we found that RocA, silvestrol, **CR-1-31-B**, **SDS-1-021**, and Zotatifin all significantly stabilize DDX21. We also found that silvestrol stabilized DDX50, a close paralog of DDX21 with 55.6% sequence similarity (66). In the presence of a polypyrimidine probe, **CR-1-31-B** and **SDS-1-021** both were found to stabilize DDX21, albeit to a lesser extent than with purine RNA (**Figure S3A-B**). **SDS-1-021** alone also stabilized the close paralogs DDX5 and DDX17, RNA helicases which overlap with 90% sequence similarity in their core domains (67). While the magnitude of stabilization for DDX5, DDX17, DDX21, and DDX50 was small in comparison to that of eIF4A and DDX3, this observation may be explained by high baseline RNA occupancy as illustrated in **Figures 3C** and **5F**. By encompassing DDX5, DDX17, DDX21, DDX50, and isoforms of DDX3 and eIF4A, our TSAR results potentially expand the rocaglate clamping spectrum from four to at least nine DDX proteins, all captured in a single profile for the synthetic rocaglate congener **SDS-1-021**.

As for other putative targets, the use of a purine or pyrimidine probe had minimal impact on non-DDX TSAR profiles. For the majority of compounds, most differentially stabilized proteins between both RNA conditions were quite close to significance thresholds such that their hit calling might reasonably fluctuate across experiments. However, we again detected stabilization of PMPCA and, for **SDS-1-021**, PMPCB, both subunits of mitochondrial processing peptidase (MPP) which cleaves signal sequences from newly imported mitochondrial proteins (68). This paired stabilization/destabilization suggests that some rocaglates disrupt the MPP complex, providing a functional link to the altered mitochondrial proteins as seen in our live-cell PISA experiment (**Figure S1**). Finally, in both RNA conditions, we observed Zotatifin-induced stabilization of dihydrofolate reductase (DHFR), a well-characterized cancer and autoimmune disease target (69).

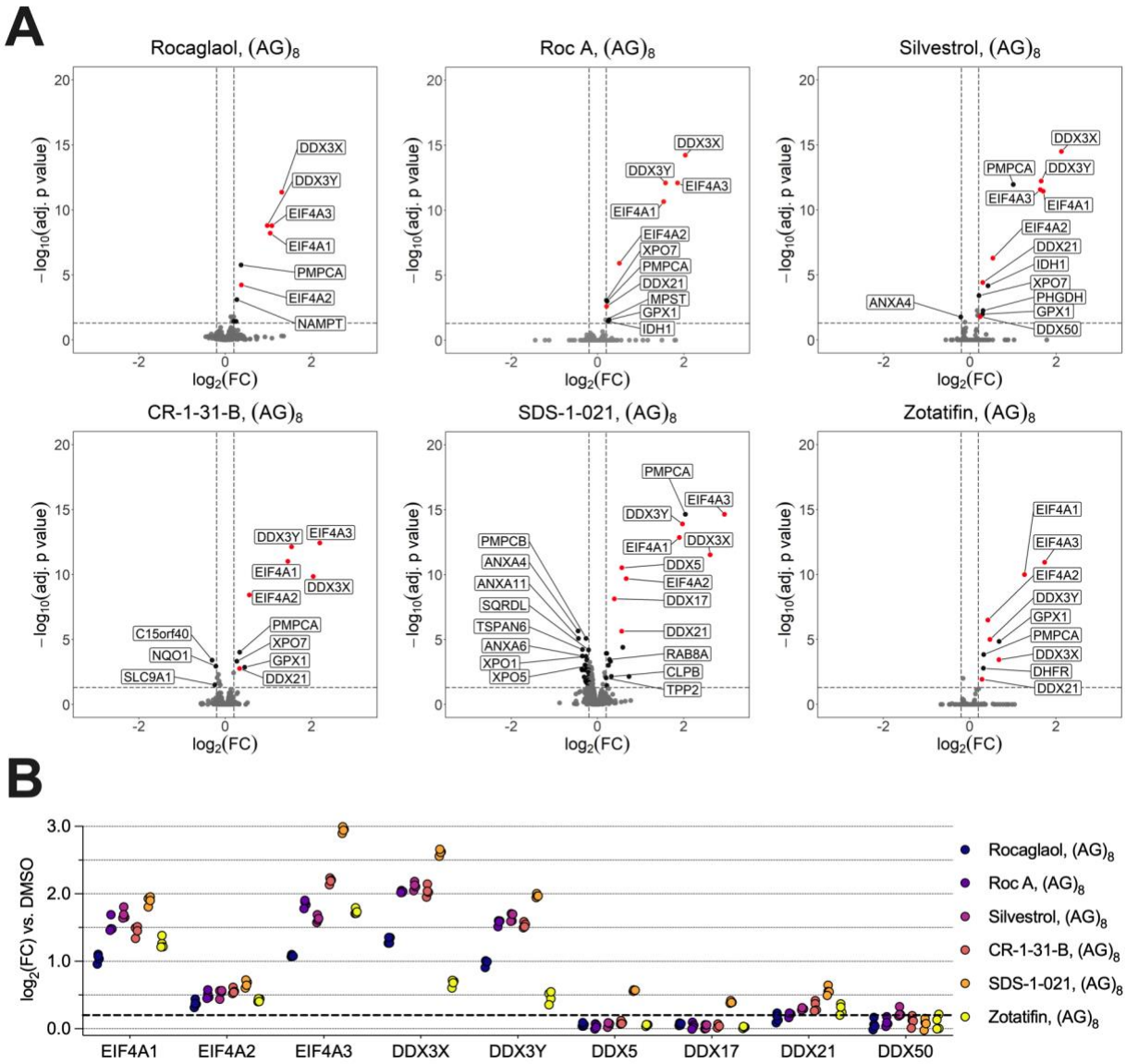

Figure 7. **TSAR profiling with a panel of rocaglates. (A)** A549 cell lysate was pre-loaded with AMP-PNP (1 mM) and $(AG)_8$ RNA (1 μM) and treated with a panel of naturally occurring (top row) and synthetic (bottom row) rocaglates (10 μM) (n = 4) before assay. Volcano plots depict differentially stabilized proteins with significant DDX proteins colored red and other significant proteins colored black. The x-axis indicates log-fold change in protein abundance in compound-treated samples. The dashed lines indicate significance thresholds ($|\log_2 FC| > 0.2$ and adj. p value ≤ .05). **(B)** Extracted fold-change values for selected DDX proteins stabilized by rocaglates derived from two separate experiments. The dashed line indicates the significance threshold ($|\log_2 FC| > 0.2$). Experiments were run using the same batch of cell lysate.

Limited-proteolysis mass spectrometry with synthetic rocaglates

Motivated by the potential of an expanded rocaglate clamping spectrum, we used a complementary target identification method, limited proteolysis-mass spectrometry (LiP-MS), to

validate some of our key TSAR findings. LiP-MS is similar to the widely used drug affinity responsive target stability (DARTS) assay (70), which reports on ligand-induced changes to proteolytic cleavage patterns; DARTS traditionally employs immunoblot detection, whereas LiP-MS increases throughput and limits user bias *via* untargeted mass spectrometry detection (49). In principle, LiP-MS exploits ligand-induced conformational changes that differentially expose or shield a target protein from limited proteolysis by a non-specific protease, such as proteinase K. After a brief incubation, the non-specific protease is heat-inactivated and samples are subjected to standard tryptic digestion. Compound and DMSO-treated samples are compared at the peptide level, and differentially quantified peptides implicate their parent proteins as putative targets.

We performed three independent LiP-MS experiments with a subset of synthetic rocaglates**: CR-1-31-B**, **SDS-1-021**, and Zotatifin (10 μM each). Based on our TSAR screens, we tested each compound in A549 lysate pre-loaded with AMP-PNP (1 mM) and $(AG)_8$ RNA (1 μM). After an equilibrating incubation with the test compound or DMSO, samples were subjected to limited proteolysis with proteinase K, followed by heat inactivation. We processed the samples through a bottom-up proteomics workflow using isobaric (TMTpro) multiplex labeling reagents and submitted them for LC-MS/MS analysis. Representative volcano plots for each experiment are provided in **Figure 8**.

As expected, all three compounds altered the proteolytic profiles of eIF4A1, eIF4A2, and eIF4A3 which resulted in multiple differentially abundant peptides for each isoform. DDX3X and DDX3Y peptides were among the most affected by **CR-1-31-B** and **SDS-1-021**, but not Zotatifin, consistent with our TSAR results showing Zotatifin as the weakest DDX3 stabilizer (**Figure 7B**). In **CR-1-31-B**-treated samples, we observed one differentially abundant unique peptide each from DDX21 (STYEQVDLIGK) and DDX5 (TLSYLLPAIVHINHQPFLER) (**Figure 8A**). While the DDX21 finding aligns with DDX21 stabilization shown in **Figures 7** and **S3**, the DDX5 finding diverges from our TSAR result. Interestingly, we also observed a single differential peptide derived from methylphosphate capping enzyme (MEPCE) which, along with DDX21, is known to bind the 7SK snRNP (59, 71). Alterations to MEPCE and DDX21 may indicate that rocaglates clamp the subpopulation of DDX21 molecules bound to endogenous ribonucleoprotein complexes, providing a starting point for future studies of DDX21 clamping. For **SDS-1-021**, we detected changes to one peptide each from DDX5 (FGNPGEK) and DDX50 (SLASVSYAAVDFFRPSAQR), but not DDX17 or DDX21 (**Figure 8B**). Notably, Zotatifin treatment resulted in one differentially abundant peptide from DDX21 (TAITVEHLAIK), a finding that aligns with our TSAR data (**Figure 8C**). Strikingly, of the 18 differentially abundant peptides detected in the Zotatifin experiment, seven belonged to DHFR. Nevertheless, in conjunction with our TSAR data, these LiP-MS results further implicate DDX3Y, DDX5, DDX21, and DDX50 as DEAD-box helicase leads for expansion of the rocaglate clamping spectrum.

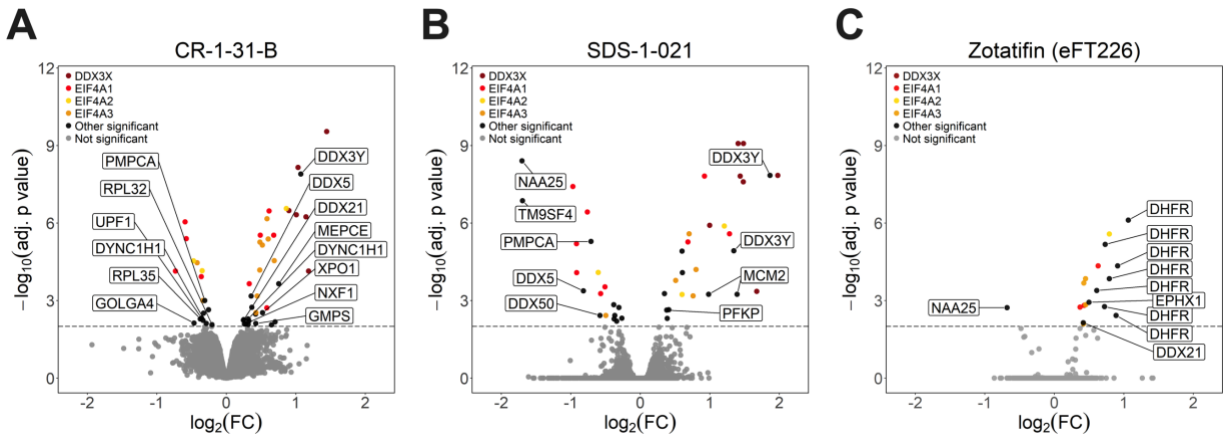

Figure 8. **Limited proteolysis-mass spectrometry with synthetic rocaglates.** Results obtained for **(A) CR-1-31-B**. **(B) SDS-1-021**. **(C)** Zotatifin (**eFT226**). A549 cell lysate was pre-loaded with AMP-PNP (1 mM) and $(AG)_8$ RNA (1 μM) and treated with a synthetic rocaglate (10 μM) or DMSO (n = 6), then subjected to limited proteolysis with proteinase K. The volcano plots are labeled with proteins corresponding to tryptic peptides that were differentially abundant between compound- and DMSO-treated samples. Unique peptides stemming from previously established DDX targets are colored in shades of red, orange, or yellow but are not labeled; unique peptides stemming from other significant proteins are labeled by protein. The dashed line indicates the statistical significance threshold (adj. p value ≤ .01).

Fluorescence polarization assays with recombinant DDXs

To firmly establish additional DDXs as direct rocaglate targets, we employed a previously developed fluorescence polarization (FP) assay using a 5'-fluorescein amidite (5'-FAM)-labeled $(AG)_8$ RNA probe (25). After successful production of recombinant eIF4A1, eIF4A3, DDX3X, DDX21, and DDX50, we used FP to evaluate our panel of rocaglates for their ability to clamp these proteins to labeled polypurine RNA, reported as a change in polarized fluorescence (ΔmP) relative to DMSO controls. Predictably, all compounds induced clamping of eIF4A1 to RNA, with generally weaker but detectable clamping of eIF4A3 (**Figure 9**). Strikingly, DDX21 and DDX50 clamped purine RNA to some extent in the presence of most compounds. This effect was the most profound for **SDS-1-021** which was the strongest clamper for all proteins tested. RocA-induced clamping of DDX3X was effectively undetectable in our hands, though **CR-1-31-B**, silvestrol, and **SDS-1-021** clamped DDX3X with moderate to high affinity. Results for Zotatifin largely echoed TSAR and LiP-MS data, with moderate clamping of DDX21 and complete inactivity against DDX3X observed. These results establish DDX21 and DDX50 as tractable DEAD-box helicase targets for future rocaglate medicinal chemistry campaigns.

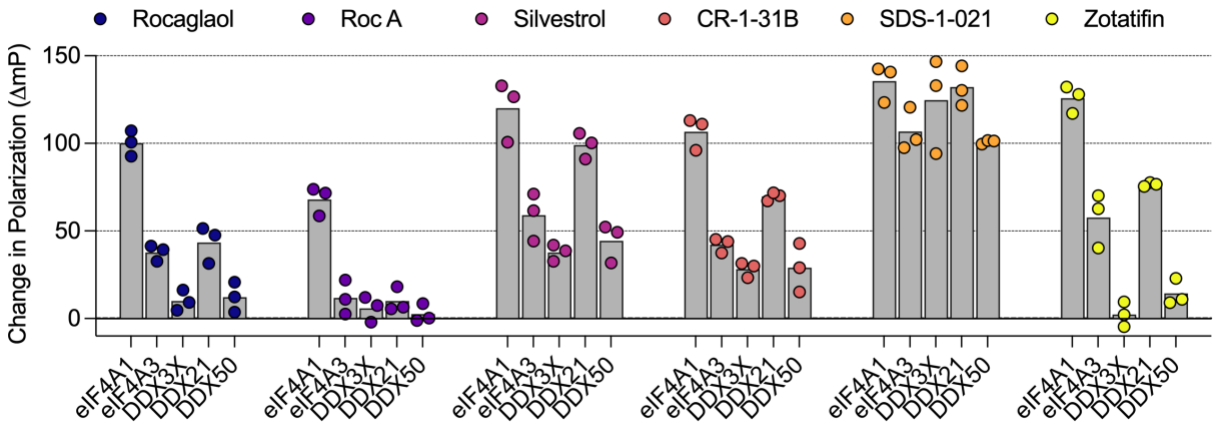

Figure 9. Fluorescence polarization with a panel of rocaglates. Recombinant DDX proteins were incubated with a 5'-FAM-labeled $(AG)_8$ RNA probe, then treated with test compound or DMSO (n = 3). Polarized fluorescence emission is measured in a polarimeter, and the DMSO-treated baseline is subtracted from compound-treated polarization to derive the compound-induced change in fluorescence polarization (ΔmP). Bars indicate mean values.

Computational modeling of rocaglate binding to DDX proteins

The heterogeneity of target profiles observed across the rocaglate variants tested raises the intriguing possibility of rationally designing rocaglates to specifically target members of the DDX family. To that end, we wanted to understand the molecular basis for Zotatifin's apparent targeting away from DDX3X as compared to other synthetic rocaglates. Zotatifin is highly structurally similar to **CR-1-31-B** (**Figure 10A**), with a nitrogen replacing *C*7 of the A-ring, a nitrile substituent at the *C*4' position of the B-ring, and an *N*,*N*-dimethylaminomethylene substituent at the *C*2-position. We first used conventional Glide docking (72, 73) to model both **CR-1-31-B** and Zotatifin into their shared target, eIF4A1, using a published RocA-$(AG)_5$-eIF4A1 X-ray crystal structure (PDB ID: 5ZC9). Both docking exercises showed the respective ligands bound in a comparable position to RocA (hereafter referred to as the "canonical" rocaglate pose), with tightly sandwiched π-stacking interactions between the A- and B-rings and $(AG)_5$ RNA. Beyond ligand-RNA interactions, RocA has been shown to engage in limited contacts with eIF4A1 itself, the two most prominent being a hydrogen bond between the RocA *C*2 amide carbonyl and eIF4A1 Gln195, and a parallel-displaced π-stacking interaction between the RocA C-ring and eIF4A1 Phe163 (33). Both interactions were fully recapitulated in the top eIF4A1 docking pose for **CR-1-31-B** (Glide Gscore: -8.170 kcal/mol) (**Figures 10B** and **S4A**). For the top Zotatifin-eIF4A1 pose (Glide Gscore: -8.240 kcal/mol) (**Figures 10C** and **S4B**), the expected π-stacking to Phe163 was also observed. Interestingly, while Zotatifin lacks a carbonyl at the *C*2 position, docking predicted the lone pair of the *C*2 dimethylamino nitrogen to sit 2.2 Å from the nearest Gln195 sidechain proton, indicative of a strong hydrogen bond.

To better understand the molecular basis for their differential targeting, we next attempted to model the two ligands into DDX3X. Here, we used an X-ray structure of DDX3X in a "rocaglate-competent" post-unwound configuration (PDB: 7LIU), in which the helicase is bound to a DNA:RNA hybrid. Unfortunately, conventional (flexible-ligand/rigid-receptor) Glide docking failed to produce the canonical rocaglate pose for either **CR-1-31-B** or Zotatifin into this structure. Consequently, we opted to deploy Schrödinger's flexible-ligand/flexible receptor Induced Fit Docking (IFD) workflow (74) given that receptors are well-precedented to undergo subtle

conformational changes to accommodate ligand binding (75). IFD modeling, which maintains a rigid protein backbone while allowing flexibility of sidechain residues, allows for structural adjustments at the putative rocaglate binding site that may serve to both avoid steric clashes and access new favorable receptor-ligand binding interactions.

Gratifyingly, the top-scored IFD poses for neutral **CR-1-31-B** (**Figures 10D** and **S4C**) and Zotatifin (**Figure 10E**) docked into DDX3X both achieved the canonical rocaglate pose, albeit with different predicted binding affinities (Glide scores: -6.539 kcal/mol for **CR-1-31-B** vs. -4.818 kcal/mol for Zotatifin). For both ligands, IFD predicted π-stacking interactions between the rocaglate A- and B-rings to C704 and G705 of the RNA:DNA hybrid, respectively. In the case of **CR-1-31-B**, we also observed a hydrogen bond between the carbonyl group of the *C*2-hydroxamic ester and the sidechain of DDX3X Gln360 (**Figure S4C**) (28), a residue analogous to eIF4A1's Gln195 (**Figure S4D**). In contrast, for Zotatifin no interactions were observed with Gln360. Due to slight positional differences for the ligand core across the two poses (**Figure S4E**), in the Zotatifin-DDX3X IFD structure the *C*2-pendant amine is turned away from Gln360, eliminating any potential to form a hydrogen bond with this key rocaglate-binding residue (28). We postulate that this difference in ability to bind Gln360 is a key driver in the differential targeting of DDX3X by the two ligands.

In comparing the two IFD poses, we also observed significant differences in the induced protein structures for the two ligands, particularly at the receptor surfaces abutting the B-and C-rings (c.f. **Figure 10D** and **Figure 10E**). The key C-ring binding residue in eIF4A1, Phe163, corresponds to residue Val328 in DDX3X (**Figure S4D**), precluding any possibility of π-stacking. We observed that in this region, a salt bridge between DDX3X's Arg363 and Glu332 was disrupted in the induced-fit modeling with **CR-1-31-B**, but not with Zotatifin (**Figure S4C**). Proximal to the B-ring, we observed the methyl group of the **CR-1-31-B** *C*4' methoxy substituent to sit in a hydrophobic cleft lined by the β-methylenes of Val328, Asp329, and newly liberated Glu332 (**Figure 10D**); this hydrophobic interaction may also contribute to the improved predicted binding affinity for **CR-1-31-B**, in comparison to the *C*4' nitrile-bearing Zotatifin. Taken together, these modeling experiments provide a potential structural basis for the experimentally observed differential targeting of DDX3X by **CR-1-31-B** and Zotatifin.

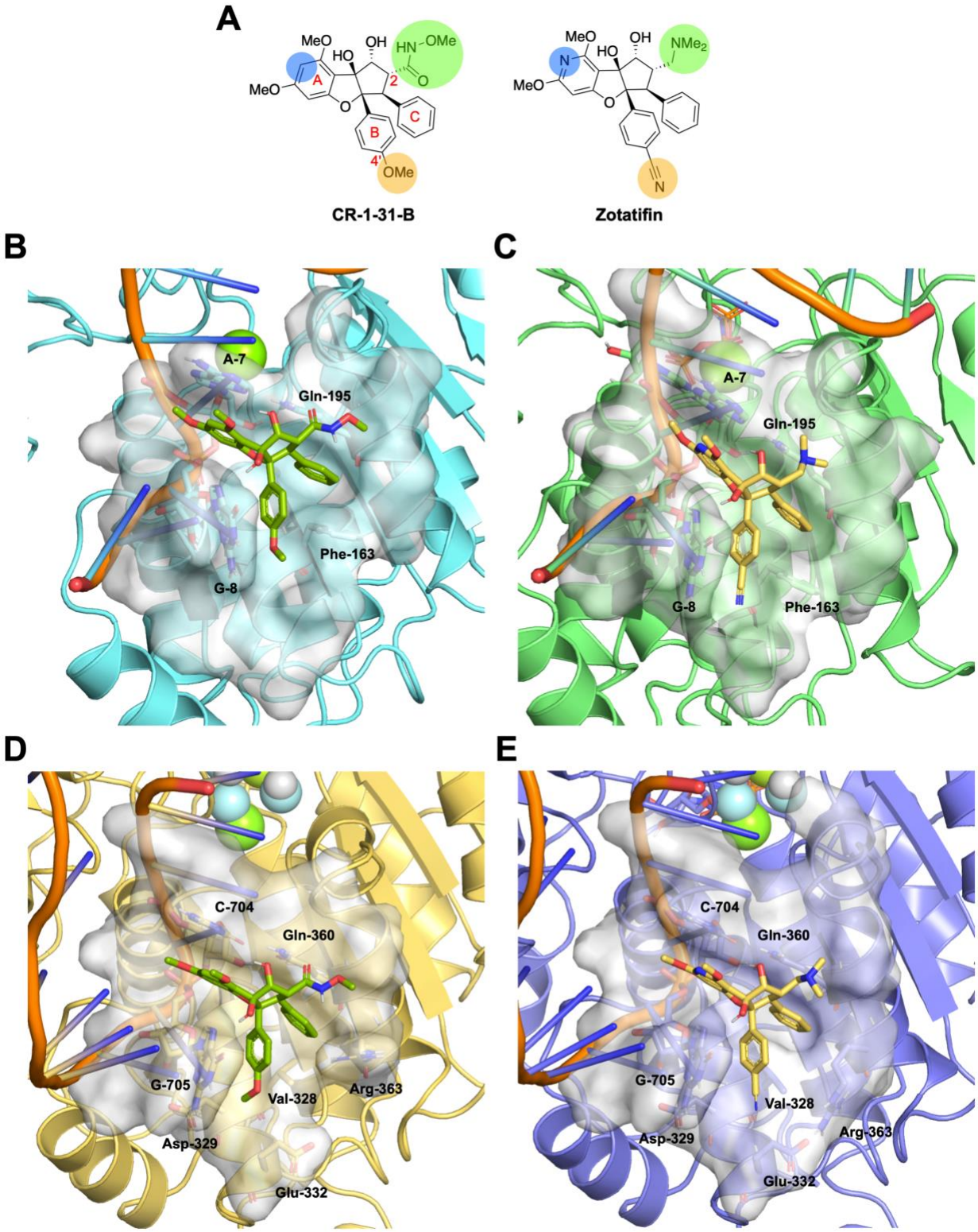

Figure 10. Docking of synthetic rocaglates into eIF4A1 and DDX3X. Rocaglate binding was analyzed *via* computational docking of **CR1-31-B** and Zotatifin (**eFT226**) into X-ray crystal structures for eIF4A1 bound to $(AG)_5$ RNA (PDB: 5ZC9), and DDX3X bound to an RNA-DNA hybrid (PDB: 7LIU). **(A)** Chemical structures of **CR-1-31-B** and Zotatifin with key structural

differences highlighted. **(B)** Pose for **CR-1-31-B** bound to an eIF4A1-RNA structure (PDB: 5ZC9) obtained from rigid-receptor docking. **(C)** Pose for Zotatifin bound to an eIF4A1-RNA structure (PDB: 5ZC9) obtained from rigid-receptor docking. **(D)** Pose for **CR-1-31-B** bound to a DDX3X-RNA/DNA structure (PDB: 7LIU) obtained from Induced Fit Docking. **(E)** Pose for Zotatifin bound to a DDX3X-RNA/DNA structure (PDB: 7LIU) obtained from Induced Fit Docking.

Discussion

To date, the rocaglate clamping spectrum has been established for at least four DDX proteins: eIF4A1, eIF4A2, eIF4A3, and DDX3X. Here, we describe TSAR (Thermal Shift Assay with ATP and RNA), a modified PISA strategy that enables detection of molecular clamping against a near proteome-wide background. Using TSAR, we provide evidence of an expanded rocaglate clamping spectrum, with validation for DDX21 and DDX50 engagement by multiple widely used rocaglates and implication of DDX3Y, DDX5, and DDX17 as rocaglate-ligandable RNA helicases. We show that these findings are conditioned upon target class-specific assay parameters, including the use of lysate additives that promote *in vitro* assembly of rocaglate receptor complexes. Our data also reveal potential non-DDX targets, providing starting points to mechanistically probe off-target effects or polypharmacology. In keeping with our overarching goal of structure-based rocaglate design, we propose a molecular basis to explain differences in DDX3X stabilization (*i.e.* affinity) through comparative docking of Zotatifin and **CR-1-31-B**. More broadly, our study provides a generalizable approach for chemical-proteomic stability screens of other types of interfacial ligands, potentially including pateamines, camptothecins, or other molecular glues, and establishes a template for identifying uncompetitive inhibitors.

Our study is not the first chemical-proteomics-based survey for rocaglate targets. It does, however, demonstrate clear advantages over prior methods, which relied on affinity enrichment (76, 77) or covalent labeling with derivatized rocaglates (28). For example, Chambers' pull-down of a biotinylated silvestrol probe did not employ additive RNA or ATP analogs, a point that Chen and coworkers also note (28). In this case, DDXs of lower affinity and abundance likely fell victim to repetitive washing in the absence of these ectopic reagents. Chen's approach, which did include RNA and AMP-PNP, involved an *O*-nitrobenzoxadiazole *(O*-NBD)-based RocA probe, which participates in covalent labeling of proximal lysines. In both examples, rocaglate derivatization has the potential to alter target binding profiles and yield spurious results. In contrast, both screens used in the current study, TSAR and LiP-MS, require no modification to the active compound, allowing for more efficient use of synthetic chemistry resources. On the other hand, stability proteomics methods have a degree of uncertainty as to whether the relevant target is sufficiently altered under the chosen perturbation conditions (*e.g.* dose, heat, proteolysis). For this reason, as others note (78), multiple complementary methods are advisable in target identification campaigns.

Our initial live-cell PISA experiment echoes common knowledge that pathway-level perturbations reflect abundance changes (*i.e.* apparent stabilization) through multiple indirect mechanisms (*e.g.* protein expression, cellular localization) (47). This is particularly salient for rocaglates, which acutely alter protein abundance through cap-dependent translation inhibition, making it unclear whether fold-change differences arise from ligand-induced stabilization or modulation of protein synthesis. On the other hand, the live-cell format informs on bioactivity downstream of target engagement. In **CR-1-31-B**-treated cells, for example, we observed alteration of proteins associated with actively translating mRNA (eIF4A1/2- and DDX3X-related), splicing machinery (eIF4A3-related), and ribosome biogenesis (DDX21-related).

In virtually any process involving RNA molecules, RNA acts as an extended scaffold for large and dynamic complexes. Since DDXs often take part in dynamic multiprotein-RNA interactions, live-cell PISA can be a particularly sensitive tool to study next-generation rocaglates that alter RNA-protein complexes independent of eIF4A or DDX3, provided that such complexes are appropriately annotated. However, even at low concentrations, rocaglates induce profound changes in cellular protein abundance and thermal stabilities, which can mask ligand-protein interactions. Thus, for the near-term identification of direct rocaglate targets, lysate-based assays appear to be more useful and warrant further future applications.

Lysis can result in an over 100-fold dilution of a cell's internal contents, leading to redistribution of important co-factors and substrates away from their cognate proteins. Accordingly, we detected maximal thermal stabilization of **CR-1-31-B** and **CMLD012824** targets in lysates replenished with both an ATP analog and a purine RNA substrate. A recent study noted divergence in calcium-induced thermal shift measurements for 2,4-dienoyl-CoA reductase (DECR1) between crude lysate and intact mitochondria, attributing the difference to insufficient levels of DECR1 substrate and cofactor in lysate (48). Our study supports a similar conclusion and reiterates the need to account for common cofactors and representative substrates for successful capture of complex binding modes.

While a broadly applicable biomolecule cocktail may yield further improvements for stability proteomics assays, we note that when evaluating additives in pilot studies, low stabilization by a primary ligand does not preclude high subsequent stabilization by a secondary ligand. For example, AMP-PNP and $(AG)_8$ RNA negligibly affected eIF4A and DDX3X stability on their own or in combination (**Figures 3C and 5F**) but enabled relatively large fold-changes upon rocaglate treatment. This observation reflects rocaglates' unique ability to stabilize transient RNA-protein interactions. Inversely, prematurely saturating DDXs with additive RNA, either with high starting concentrations or with a high affinity probe, can be detrimental to assay sensitivity. Compared to using 1 μM $(AG)_8$ RNA, 30 μM $(AG)_8$ RNA resulted in a nearly 50% reduction in **CMLD012824**-induced fold-change for DDX21 (**Figure 6B**). Optimal RNA concentration appears to be protein-specific and may require careful titration or trade-offs in sensitivity for different DDXs.

One way to mitigate sensitivity tradeoffs is through informed selection of heating temperatures. Others have demonstrated that higher temperature ranges can magnify stabilization readouts, provided that the linear portion of the stability curve is captured for proteins of interest (47, 62). It was a matter of serendipity that most DDXs have half-maximal melting points between those of DDX3X and eIF4A2 (**Figure 4A**) – this helped us infer that the temperatures we tested were representative of the target class. To verify this in the absence of a pan-DDX rocaglate, we performed a second temperature range experiment using elevated concentrations of AMP-PNP and $(AG)_8$ RNA, which forced protein engagement. We did not evaluate an isothermal assay, though we expect the format to be more sensitive and efficient in focused designer rocaglate applications. For such applications, investigators may find targeted pathway proteomics methods particularly useful (79).

Why does AMP-PNP offer improved assay performance over the native ligand ATP? Structural studies of ATPases often employ non-hydrolysable ATP analogs to trap enzymes in a pre-hydrolytic state (80). Others have shown that DDX-RNA complexes dissociate rapidly, with half-lives of seconds to a few minutes in the presence of ATP, whereas AMP-PNP-bound complexes can persist for hours (30). This difference likely manifests as a suboptimal distribution of DDX species in ATP-treated lysates, given that only RNA-bound DDXs can act as rocaglate receptors. Whether AMP-PNP is the most useful ATP analog for investigations with different RNA additives remains a topic for future investigations. In this study, we only compared a small panel of single stranded RNA molecules. In theory, rocaglates can engage any individual DDX-RNA

complex bound to such a simple RNA, since the presentation of purines in the rocaglate binding site remains a constant. We speculate that experiments with more complex RNA molecules (*i.e.* highly structured RNA) (81) may benefit from the use of ATP, as it could allow DDX-RNA complexes to dissociate and reassociate until a rocaglate-competent binding site is formed. Investigations around the nucleic acid structural preferences of different DDX proteins may shed light on biological processes and disease states ripe for rocaglate targeting.

In the current study, we found that a simple single-stranded RNA probe was sufficient to profile known rocaglate targets and generate leads for future DDX clamping projects. Building on Chen and coworkers' DDX3X study (28), who showed RocA clamps polypurine RNA to DDX3X with a dissociation constant of 420 nM, our TSAR, LiP-MS, and FP results show that DDX3X clamping is a common feature of several high profile rocaglates. The observation that DDX3X was thermally stabilized using TSAR by RocA, rocaglaol, and Zotatifin while effectively null by FP points to the sensitivity of TSAR-based DDX3X stabilization measurements but warns against data overinterpretation. On the other hand, weak DDX3X engagement in recombinant protein FP assays may simply indicate that the lysate-based system contains yet additional co-factors that promote target engagement.

We also found that DDX3Y, a male-specific paralog that shares 90% sequence similarity with DDX3X (82), is stabilized in parallel with DDX3X in both TSAR and LiP-MS, a finding afforded by our use of male-derived cell lysate. The apparent unity between DDX3X and DDX3Y targeting, at least among our compound panel, urges thorough structural evaluation for groups embarking on paralog-specific rocaglate discovery (83).

Regarding novel DDX proteins, we establish DDX21 and DDX50 as *bona-fide* rocaglate targets amenable to RNA clamping. DDX21 has reported roles in ribosome biogenesis, innate immunity, and glucose sensing, among several others (36, 59). Its close paralog DDX50 was recently characterized as a viral sensor involved in Dengue virus infection (66). Their sequence similarity may suggest parallel targeting as with DDX3 isoforms, though closer study is warranted at this time. Thus far, we have not had the opportunity to confirm DDX5 and DDX17 engagement using recombinant protein, but their high degree of core domain similarity may suggest a parallel targeting effect as well.

We also note that Zotatifin, an eIF4A-selective rocaglate that appears to have been successfully tuned away from DDX3, stabilized DDX21 and DHFR in both TSAR and LiP-MS assays. DHFR, a historically well-studied cancer and auto-immune target, is inhibited by folate antagonists (*e.g.* methotrexate), which have been shown to also possess *in vitro* antiviral activity (69, 84-86). Given Zotatifin's status as a clinical candidate for both ER+ breast cancer and SARS-CoV-2 infection, our findings may warrant follow-up to determine whether DDX21 and DHFR contribute to Zotatifin's efficacy or pose liabilities.

Zotatifin was optimized for eIF4A inhibition in a campaign that also targeted improved drug-like properties through reduced lipophilicity and increased aqueous solubility, which was presumably a key motivation behind installing the *C*2 tertiary amine, *C*4' nitrile, and nitrogenated A-ring. However, our modeling and experimental data suggest that these modifications also provided a ligand relatively selective for eIF4A. Based on our modeling, we posit that for Zotatifin, an *in silico*-predicted loss of Gln360 H-bonding capability at *C*2 significantly hampers DDX3X engagement. In the case of **CR-1-31-B**, however, our modeling predicts a retained interaction with Gln360, in combination with additional binding interactions arising from Arg363-Glu332 salt bridge disruption. For **CR-1-31-B**, these collective interactions appear to sufficiently offset the loss of π-π stacking arising from the Phe→Val mutation, a phenomenon that we expect is extendable to other *C*2 carbonylated DDX3X-targeting rocaglates such as silvestrol. While not directly interrogated by our modeling, we note that is also possible that subtle electronic differences in the

pyridine A-ring of Zotatifin compared with phenyl A-ring of **CR-1-31-B** may impact the π-stacking interactions with polypurine RNA in the ternary complex (7). While the predicted ligand-induced DDX3X conformational changes must still be validated experimentally, this modeling study nonetheless introduces the potential to strategically tune rocaglate targeting toward or away from specific helicases using rational, structure-based drug design.

Pre-loading cell lysates with the constituents of rocaglate receptors provides the basis, in theory, for a pan-DDX clamping assay – analogous to fluorescence polarization, but horizontally integrated to cover all targets of interest in a single shot. We anticipate that TSAR-inspired chemical-proteomic screens will accelerate future studies in this field and will aid in the identification of novel compounds targeted towards RNA helicases including DDX21, DDX50, DDX3Y, DDX5, and DDX17. Currently, the main barrier to this goal is a paucity of useful data to inform structure-based rocaglate design. Using TSAR and allied techniques, we hope to catalyze activity in rocaglate drug discovery by shifting medicinal chemistry focus toward actionable DDX targets, opening the door for next generation RNA-protein molecular clamps.

Acknowledgements

We dedicate this article to the memory of Professor Jerry Pelletier, a pioneer in the field of RNA biology whose work laid the foundation for rocaglate drug discovery. We thank the National Institutes of Health (R35 GM 118173) for financial support and for support in funding an ultra-high precision mass spectrometer (S10OD026807). We also thank the National Institute of General Medical Sciences (T32 GM008541) and the Canadian Institute of Health Research (PJT-186015, PJT-183610) for additional funding. We thank Michelle Nguyen and Dr. John Connor (BU) for providing A549 cells. CETSA ® (*i.e.* PISA, TSAR) data was generated under an agreement with Pelago Bioscience AB who own the CETSA patent family. Computational work at Boston University reported in this paper was performed on the Shared Computing Cluster (SCC) which is administered by Boston University's Research Computing Services.

Data Availability

The live cell PISA mass spectrometry proteomics data have been deposited to the ProteomeXchange Consortium via the PRIDE (87) partner repository with the dataset identifier PXD051420 and 10.6019/PXD051420. The lysate-based TSAR and LiP-MS mass spectrometry proteomics data have been deposited to the ProteomeXchange Consortium via the PRIDE partner repository with the dataset identifier PXD051539. PISA and TSAR experiments were quantified on the basis of two unique peptide identifications, but LiP-MS experiments were analyzed at the individual peptide level; accordingly, in addition to the PRIDE depositions listed above, we have uploaded annotated spectra from LiP-MS experiments to MS-Viewer for streamlined access. These spectra can be viewed through the MS-Viewer tool using the following access codes (also provided in the PRIDE upload):

LiP-MS experiment 1 with CR-1-31-B: tcdvvuilc4

LiP-MS experiment 2 with SDS-1-021: fkphqcsnxd

LiP-MS experiment 3 with Zotatifin: v0xndsuc60

Supplemental Data

This article contains supplemental figures. All quantitative results (*e.g.* fold-changes) are available through the PRIDE accession numbers above.

Declaration of Interests

JL and AC are employees of Pelago Bioscience AB, the owner of the CETSA® family of patents. AE is a cofounder of the biotech startup Prisma Therapeutics, but states no conflict of interest. All other authors declare no competing financial interests or personal relationships that could have appeared to influence the work reported in this paper.

CRediT Authorship Contribution Statement

Stanley I. Goldstein: Conceptualization, Methodology, Validation, Formal Analysis, Investigation, Resources, Data Curation, Writing – Original Draft, Writing – Review & Editing, Visualization, Supervision, Project Administration. **Alice C. Fan:** Formal analysis, Investigation, Writing – Review & Editing. **Zihao Wang:** Formal Analysis, Investigation, Writing – Original Draft, Writing – Review & Editing, Visualization. **Sai K. Naineni:** Formal Analysis, Investigation. **Johan Lengqvist:** Formal Analysis, Investigation**. Alexey Chernobrovkin:** Formal Analysis, Data Curation, Writing – Review & Editing**. Steve B. Garcia-Gutierrez:** Conceptualization, Methodology, Investigation**. Regina Cencic:** Formal Analysis, Writing – Review & Editing. **Kesha Patel:** Resources. **Sidong Huang:** Writing – Review & Editing. **Lauren E. Brown:** Validation, Formal Analysis, Writing – Original Draft, Writing – Review & Editing, Supervision. **Andrew Emili:** Conceptualization, Resources, Writing – Review & Editing, Supervision, Funding Acquisition. **John A. Porco, Jr.:** Conceptualization, Resources, Writing – Review & Editing, Supervision, Project Administration, Funding Acquisition.

Supplementary Figures

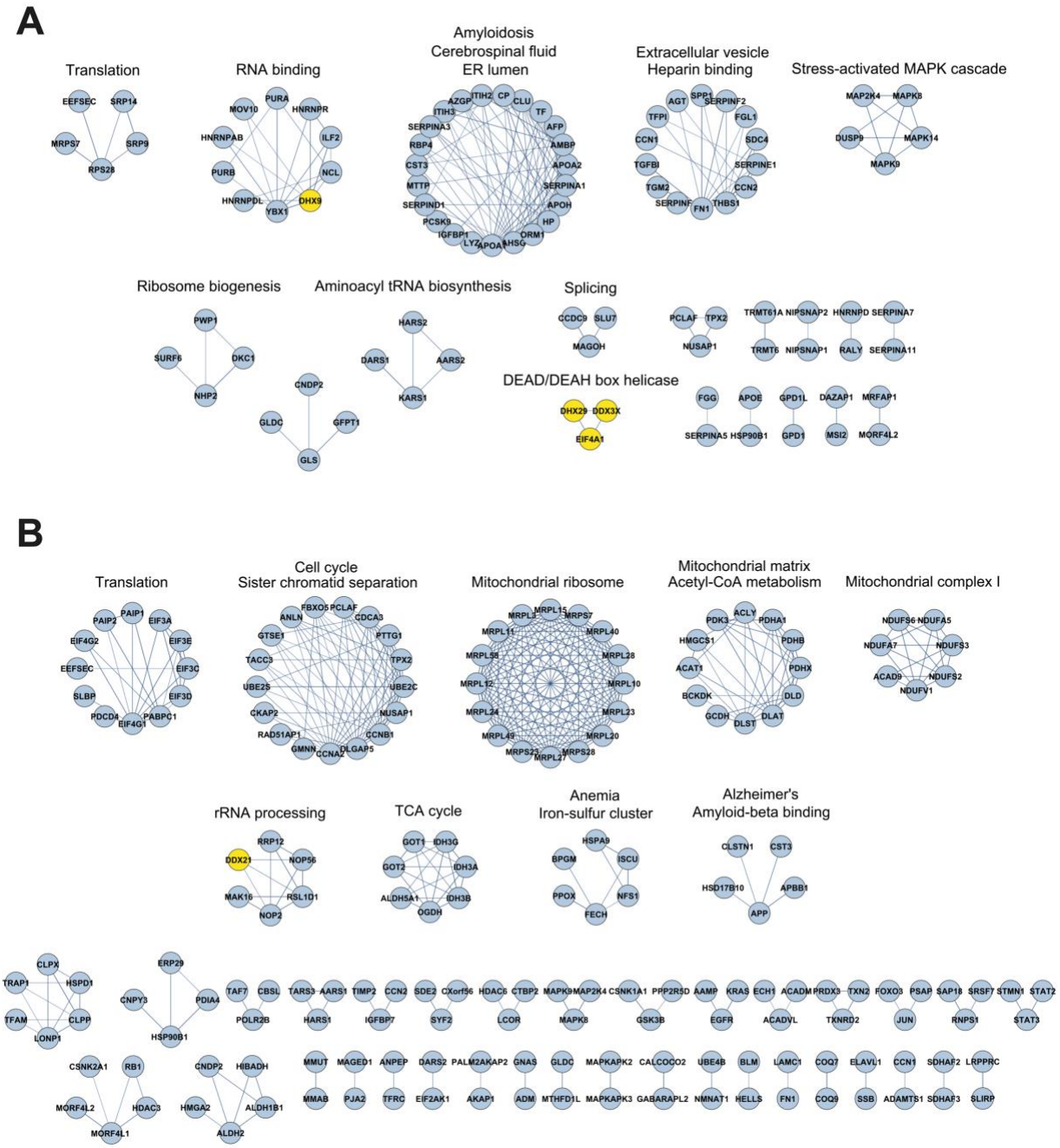

Figure S1. Network of significantly altered proteins in CR-1-31-B live-cell PISA. Significantly altered proteins (adj. p value ≤ .01) in HepG2 **(A)** and HEK293 **(B)** cells treated with **CR-1-31-B** (3 μM) and assayed via live-cell PISA. Full networks were first constructed using STRING-DB (db version 12.0) with a minimum required interaction score of 0.7 using textmining, experiments, databases, and co-expression as active interaction sources. Networks were imported into Cytoscape, clustered (MCL), and singletons removed. The network was first organized using a degree sorted circle layout, then groupings were organized manually. Default Cytoscape settings were used throughout. Selected clusters were analyzed for functional enrichments. Manually selected functional enrichments are listed above selected clusters. DDX/DHX helicases that were significantly altered are highlighted in yellow.

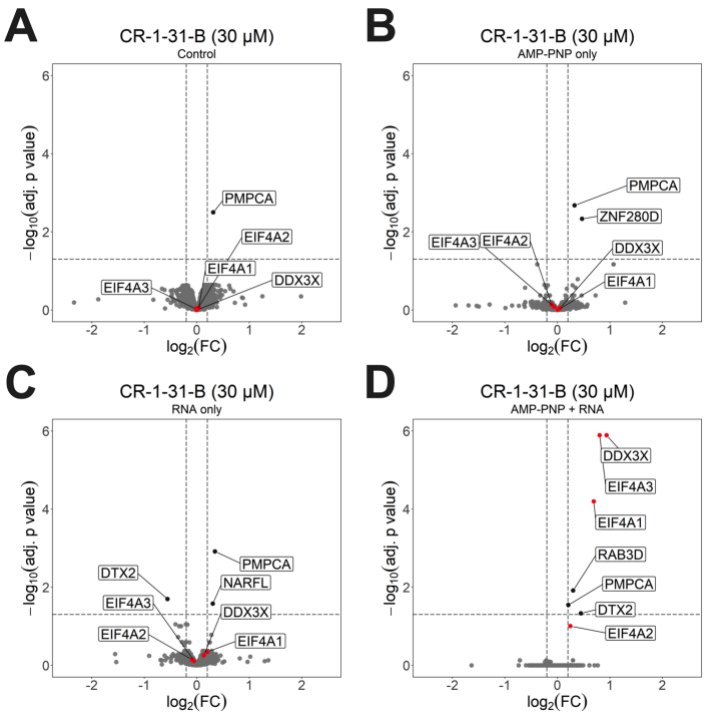

Figure S2. Additive helicase co-substrates promote thermal stabilization of rocaglate targets. HEK-293 cell lysates were left as-is **(A)** or pre-loaded with AMP-PNP (1 mM) **(B)**, $(AG)_8$ RNA (1 μM) **(C)**, or both (**D)** and treated with **CR-1-31-B** (30 μM) or DMSO (n = 2), then assayed for **CR-1-31-B**-induced thermal stabilization. The volcano plots depict differentially stabilized proteins, with known DEAD-box protein targets colored red. The x-axis indicates log-fold change in protein abundance in compound-treated samples. The dashed lines indicate significance thresholds ($|\log_2 FC| > 0.2$ and adj. p value ≤ .05).

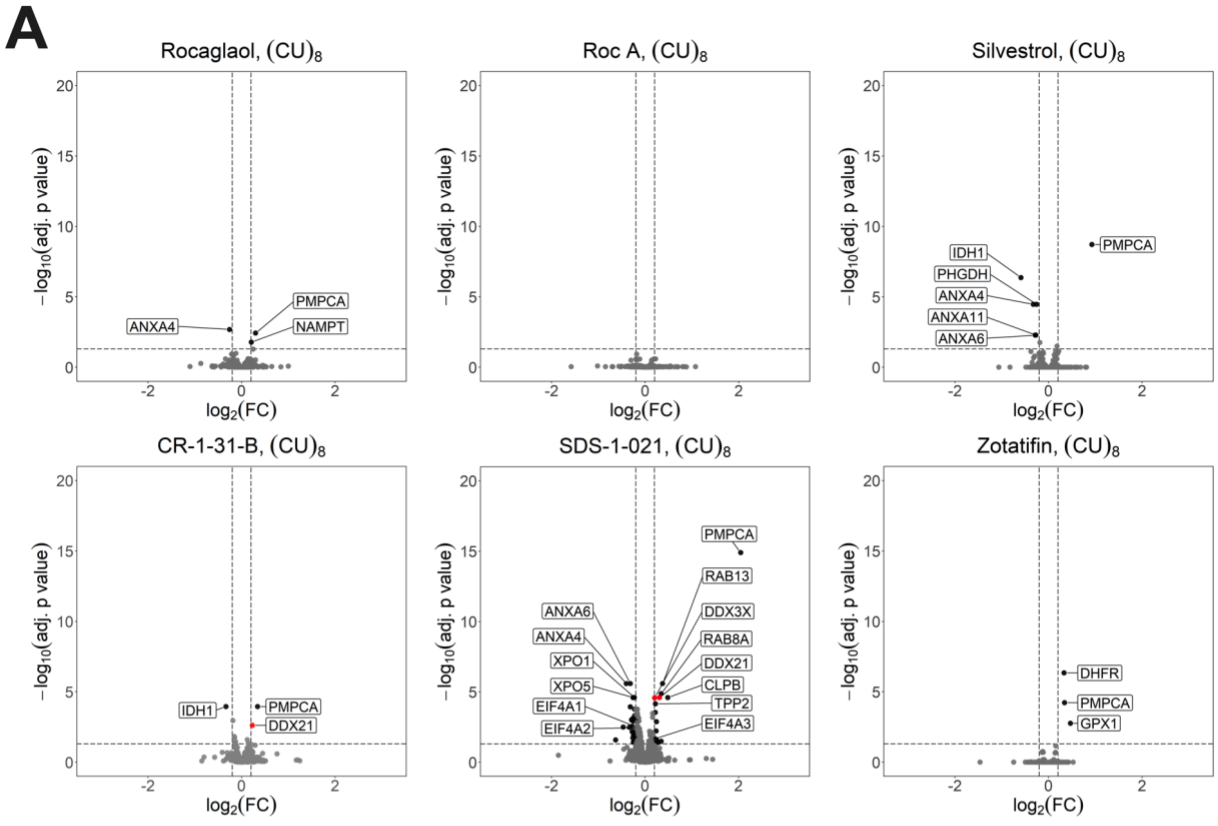
A
Rocaglaol, (CU)8
Roc A, (CU)8
Silvestrol, (CU)8
CR-1-31-B, (CU)8
SDS-1-021, (CU)8
Zotatifin, (CU)8
−log10(adj. p value)
log2(FC)
ANXA4
PMPCA
NAMPT
IDH1
PHGDH
ANXA11
ANXA6
DDX21
RAB13
DDX3X
RAB8A
CLPB
TPP2
EIF4A3
XPO1
XPO5
EIF4A1
EIF4A2
DHFR
GPX1

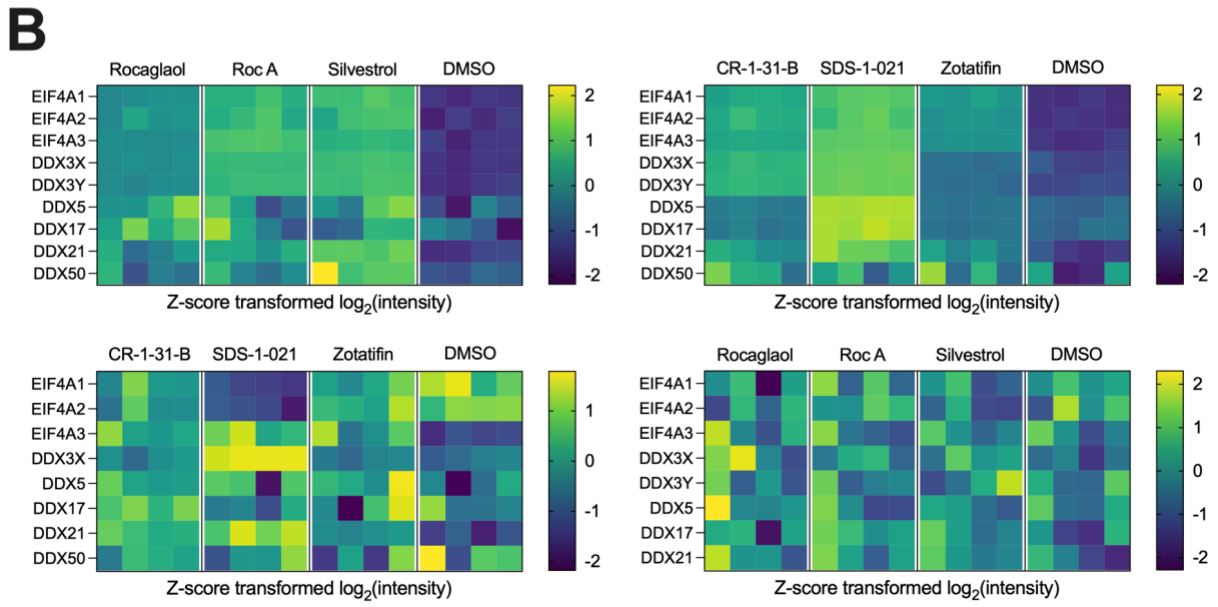
B
Rocaglaol
Roc A
Silvestrol
DMSO
CR-1-31-B
SDS-1-021
Zotatifin
EIF4A1
EIF4A2
EIF4A3
DDX3X
DDX3Y
DDX5
DDX17
DDX21
DDX50
Z-score transformed log2(intensity)

Figure S3. TSAR profiling with a panel of rocaglates. (A) A549 cell lysate was pre-loaded with AMP-PNP (1 mM) and pyrimidine $(CU)_8$ RNA (1 μM) and treated with a panel of naturally occurring (top row) and synthetic (bottom row) rocaglates (10 μM) (n = 4) before assay. Volcano plots depict differentially stabilized proteins with significant DDX proteins colored red and other significant proteins colored black. The x-axis indicates log-fold change in protein abundance in compound-treated samples. The dashed lines indicate significance thresholds ($|\log_2 FC| > 0.2$ and adj. p value $\leq .05$). **(B)** Heat map of Z-score transformed log intensity values for all DDX proteins significantly stabilized by at least one test compound in the presence of purine or pyrimidine RNA.

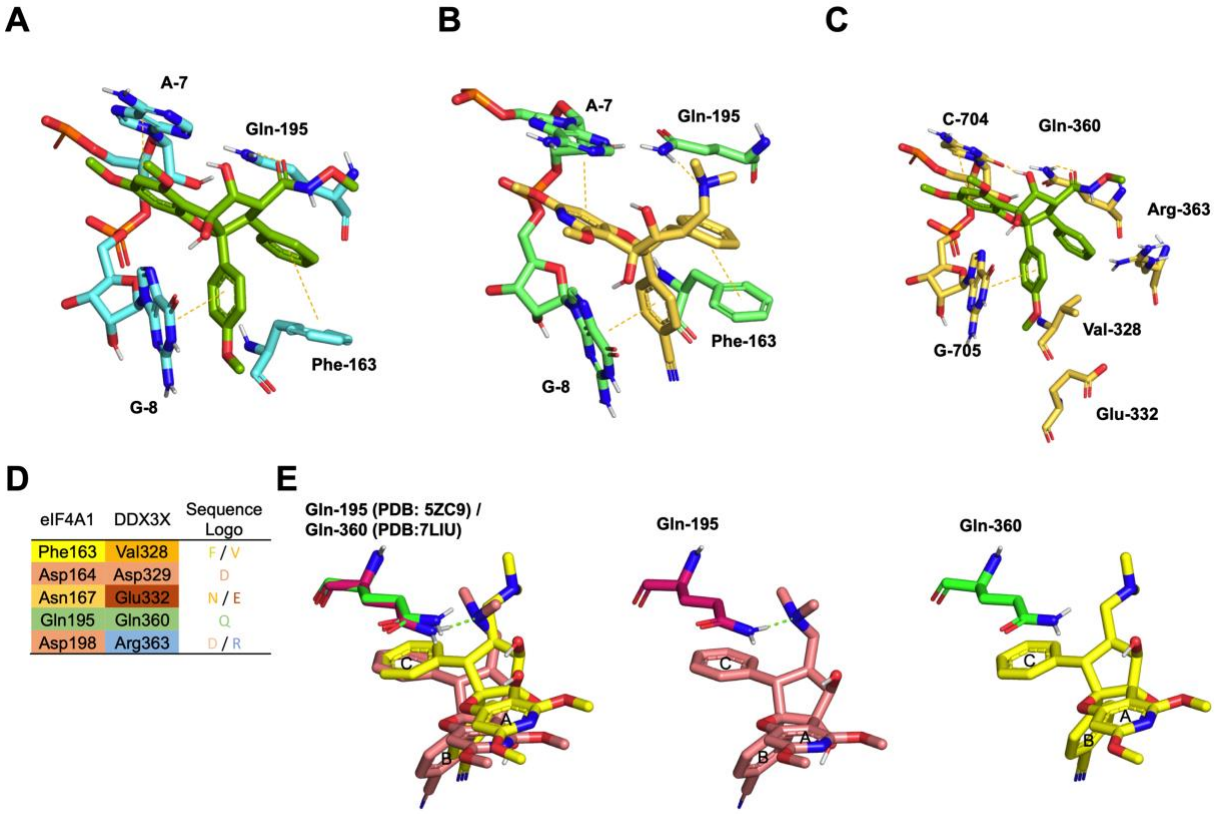

Figure S4. Poses for **CR-1-31-B** (**A**) and Zotatifin (**B**) docked into a published RocA-$(AG)_5$-eIF4A1 X-ray crystal structure (PDB ID: 5ZC9). (**C**) Induced fit docking (IFD) of **CR-1-31-B** into a DDX3X-RNA/DNA hybrid structure (PDB ID: 7LIU), with key binding interactions highlighted. (**D**) Comparison of key eIF4A1 (*left*) and DDX3X (*right*) amino acid residues at the rocaglate binding site. (**E**) An overlay of modeling results for Zotatifin docked into eIF4A1 (PDB ID: 5ZC9) and DDX3X (PDB ID: 7LIU).

References

1. Roche, S. P., Cencic, R., Pelletier, J., and Porco, J. A., Jr. (2010) Biomimetic photocycloaddition of 3-hydroxyflavones: synthesis and evaluation of rocaglate derivatives as inhibitors of eukaryotic translation. *Angew Chem Int Ed Engl.* **49**, 6533-6538

2. Rodrigo, C. M., Cencic, R., Roche, S. P., Pelletier, J., and Porco, J. A. (2012) Synthesis of rocaglamide hydroxamates and related compounds as eukaryotic translation inhibitors: synthetic and biological studies. *J Med Chem.* **55**, 558-562

3. Liu, T., Nair, S. J., Lescarbeau, A., Belani, J., Peluso, S., Conley, J. *et al.* (2012) Synthetic silvestrol analogues as potent and selective protein synthesis inhibitors. *J Med Chem.* **55**, 8859-8878

4. Wang, W., Cencic, R., Whitesell, L., Pelletier, J., and Porco, J. A., Jr. (2016) Synthesis of Aza-Rocaglates via ESIPT-Mediated (3+2) Photocycloaddition. *Chemistry.* **22**, 12006-12010

5. Zhang, W., Chu, J., Cyr, A. M., Yueh, H., Brown, L. E., Wang, T. T. *et al.* (2019) Intercepted Retro-Nazarov Reaction: Syntheses of Amidino-Rocaglate Derivatives and Their Biological Evaluation as eIF4A Inhibitors. *J Am Chem Soc.* **141**, 12891-12900

6. Zhang, W., Liu, S., Maiga, R. I., Pelletier, J., Brown, L. E., Wang, T. T., and Porco, J. A., Jr. (2019) Chemical Synthesis Enables Structural Reengineering of Aglaroxin C Leading to Inhibition Bias for Hepatitis C Viral Infection. *J Am Chem Soc.* **141**, 1312-1323

7. Ernst, J. T., Thompson, P. A., Nilewski, C., Sprengeler, P. A., Sperry, S., Packard, G. *et al.* (2020) Design of Development Candidate eFT226, a First in Class Inhibitor of Eukaryotic Initiation Factor 4A RNA Helicase. *J Med Chem.* **63**, 5879-5955

8. Nilewski, C., Michels, T. D., Xiang, A. X., Packard, G. K., Sprengeler, P. A., Eam, B. *et al.* (2020) Strategic Diastereoselective C1 Functionalization in the Aza-Rocaglamide Scaffold toward Natural Product-Inspired eIF4A Inhibitors. *Org Lett.* **22**, 6257-6261

9. Praditya, D. F., Klohn, M., Bruggemann, Y., Brown, L. E., Porco, J. A., Jr., Zhang, W. *et al.* (2022) Identification of structurally re-engineered rocaglates as inhibitors against hepatitis E virus replication. *Antiviral Res.* **204**, 105359

10. Ge, W., Ming, W., Li, Z., Tang, Y., Li, Y. N., Yang, J. *et al.* (2024) Design and Synthesis of Cytotoxic Water-Soluble Rocaglaol Derivatives against HEL Cells by Inhibiting Fli-1. *J Nat Prod.* **87**, 276-285

11. Cencic, R., Im, Y. K., Naineni, S. K., Moustafa-Kamal, M., Jovanovic, P., Sabourin, V. *et al.* (2024) A second-generation eIF4A RNA helicase inhibitor exploits translational reprogramming as a vulnerability in triple-negative breast cancer. *Proc Natl Acad Sci U S A.* **121**, e2318093121

12. Victoria, C., Schulz, G., Klohn, M., Weber, S., Holicki, C. M., Bruggemann, Y. *et al.* (2024) Halogenated Rocaglate Derivatives: Pan-antiviral Agents against Hepatitis E Virus and Emerging Viruses. *J Med Chem.* **67**, 289-321

13. King, M. L., Lin, H. C., Wang, C. B., Wang, C. T., and Leu, S. C. (1975) Antitumor Agents IV-Aglailic Acid, Dimethyl Terephthalate, and Phytosterols from Aglaia elliptifolia. *J Med Sci.* **1**, 11-21

14. Lu King, M., Chiang, C.-C., Ling, H.-C., Fujita, E., Ochiai, M., and McPhail, A. T. (1982) X-Ray crystal structure of rocaglamide, a novel antileulemic 1H-cyclopenta[b]benzofuran from Aglaia elliptifolia. *J Chem Soc, Chem Commun.*10.1039/c39820001150

15. Hwang, B. Y., Su, B. N., Chai, H., Mi, Q., Kardono, L. B., Afriastini, J. J. *et al.* (2004) Silvestrol and episilvestrol, potential anticancer rocaglate derivatives from Aglaia silvestris. *J Org Chem.* **69**, 3350-3358

16. Obermann, W., Friedrich, A., Madhugiri, R., Klemm, P., Mengel, J. P., Hain, T. *et al.* (2022) Rocaglates as Antivirals: Comparing the Effects on Viral Resistance, Anti-Coronaviral Activity, RNA-Clamping on eIF4A and Immune Cell Toxicity. *Viruses.* **14**, 519

17. Biedenkopf, N., Lange-Grunweller, K., Schulte, F. W., Weisser, A., Muller, C., Becker, D. *et al.* (2017) The natural compound silvestrol is a potent inhibitor of Ebola virus replication. *Antiviral Res.* **137**, 76-81

18. Elgner, F., Sabino, C., Basic, M., Ploen, D., Grunweller, A., and Hildt, E. (2018) Inhibition of Zika Virus Replication by Silvestrol. *Viruses.* **10**, 149

19. Henss, L., Scholz, T., Grunweller, A., and Schnierle, B. S. (2018) Silvestrol Inhibits Chikungunya Virus Replication. *Viruses.* **10**, 592

20. Muller, C., Obermann, W., Karl, N., Wendel, H. G., Taroncher-Oldenburg, G., Pleschka, S. *et al.* (2021) The rocaglate CR-31-B (-) inhibits SARS-CoV-2 replication at non-cytotoxic, low nanomolar concentrations in vitro and ex vivo. *Antiviral Res.* **186**, 105012

21. Langlais, D., Cencic, R., Moradin, N., Kennedy, J. M., Ayi, K., Brown, L. E. *et al.* (2018) Rocaglates as dual-targeting agents for experimental cerebral malaria. *Proc Natl Acad Sci U S A.* **115**, E2366-E2375

22. Chaparro, V., Leroux, L. P., Masvidal, L., Lorent, J., Graber, T. E., Zimmermann, A. *et al.* (2020) Translational profiling of macrophages infected with Leishmania donovani identifies mTOR- and eIF4A-sensitive immune-related transcripts. *PLoS Pathog.* **16**, e1008291

23. Chatterjee, S., Yabaji, S. M., Rukhlenko, O. S., Bhattacharya, B., Waligurski, E., Vallavoju, N. *et al.* (2021) Channeling macrophage polarization by rocaglates increases macrophage resistance to Mycobacterium tuberculosis. *iScience.* **24**, 102845

24. Obermann, W., Azri, M. F. D., Konopka, L., Schmidt, N., Magari, F., Sherman, J. *et al.* (2023) Broad anti-pathogen potential of DEAD box RNA helicase eIF4A-targeting rocaglates. *Sci Rep.* **13**, 9297

25. Chu, J., Zhang, W., Cencic, R., Devine, W. G., Beglov, D., Henkel, T. *et al.* (2019) Amidino-Rocaglates: A Potent Class of eIF4A Inhibitors. *Cell Chem Biol.* **26**, 1586-1593

26. Chu, J., Zhang, W., Cencic, R., O'Connor, P. B. F., Robert, F., Devine, W. G. *et al.* (2020) Rocaglates Induce Gain-of-Function Alterations to eIF4A and eIF4F. *Cell Rep.* **30**, 2481-2488

27. Ho, J. J. D., Cunningham, T. A., Manara, P., Coughlin, C. A., Arumov, A., Roberts, E. R. *et al.* (2021) Proteomics reveal cap-dependent translation inhibitors remodel the translation machinery and translatome. *Cell Rep.* **37**, 109806

28. Chen, M., Asanuma, M., Takahashi, M., Shichino, Y., Mito, M., Fujiwara, K. *et al.* (2021) Dual targeting of DDX3 and eIF4A by the translation inhibitor rocaglamide A. *Cell Chem Biol.* **28**, 475-486

29. Naineni, S. K., Cencic, R., Robert, F., Brown, L. E., Haque, M., Scott-Talib, J. *et al.* (2023) Exploring the targeting spectrum of rocaglates among eIF4A homologs. *RNA.* **29**, 826-835

30. Iwasaki, S., Floor, S. N., and Ingolia, N. T. (2016) Rocaglates convert DEAD-box protein eIF4A into a sequence-selective translational repressor. *Nature.* **534**, 558-561

31. Cencic, R., Carrier, M., Galicia-Vazquez, G., Bordeleau, M. E., Sukarieh, R., Bourdeau, A. *et al.* (2009) Antitumor activity and mechanism of action of the cyclopenta[b]benzofuran, silvestrol. *PLoS One.* **4**, e5223

32. Bordeleau, M. E., Robert, F., Gerard, B., Lindqvist, L., Chen, S. M., Wendel, H. G. *et al.* (2008) Therapeutic suppression of translation initiation modulates chemosensitivity in a mouse lymphoma model. *J Clin Invest.* **118**, 2651-2660

33. Iwasaki, S., Iwasaki, W., Takahashi, M., Sakamoto, A., Watanabe, C., Shichino, Y. *et al.* (2019) The Translation Inhibitor Rocaglamide Targets a Bimolecular Cavity between eIF4A and Polypurine RNA. *Mol Cell.* **73**, 738-748

34. Linder, P., and Jankowsky, E. (2011) From unwinding to clamping - the DEAD box RNA helicase family. *Nat Rev Mol Cell Biol.* **12**, 505-516

35. Andrisani, O., Liu, Q., Kehn, P., Leitner, W. W., Moon, K., Vazquez-Maldonado, N. *et al.* (2022) Biological functions of DEAD/DEAH-box RNA helicases in health and disease. *Nat Immunol.* **23**, 354-357

36. Holmstrom, T. H., Mialon, A., Kallio, M., Nymalm, Y., Mannermaa, L., Holm, T. *et al.* (2008) c-Jun supports ribosomal RNA processing and nucleolar localization of RNA helicase DDX21. *J Biol Chem.* **283**, 7046-7053

37. Yoneyama, M., Kikuchi, M., Natsukawa, T., Shinobu, N., Imaizumi, T., Miyagishi, M. *et al.* (2004) The RNA helicase RIG-I has an essential function in double-stranded RNA-induced innate antiviral responses. *Nat Immunol.* **5**, 730-737

38. Shih, J. W., Tsai, T. Y., Chao, C. H., and Wu Lee, Y. H. (2008) Candidate tumor suppressor DDX3 RNA helicase specifically represses cap-dependent translation by acting as an eIF4E inhibitory protein. *Oncogene.* **27**, 700-714

39. Valdez, B. C., Perlaky, L., and Henning, D. (2002) Expression, cellular localization, and enzymatic activities of RNA helicase II/Gu(beta). *Exp Cell Res.* **276**, 249-263

40. Meissner, F., Geddes-McAlister, J., Mann, M., and Bantscheff, M. (2022) The emerging role of mass spectrometry-based proteomics in drug discovery. *Nat Rev Drug Discov.* **21**, 637-654

41. Savitski, M. M., Reinhard, F. B., Franken, H., Werner, T., Savitski, M. F., Eberhard, D. *et al.* (2014) Tracking cancer drugs in living cells by thermal profiling of the proteome. *Science.* **346**, 1255784

42. Gaetani, M., Sabatier, P., Saei, A. A., Beusch, C. M., Yang, Z., Lundstrom, S. L., and Zubarev, R. A. (2019) Proteome Integral Solubility Alteration: A High-Throughput Proteomics Assay for Target Deconvolution. *J Proteome Res.* **18**, 4027-4037

43. Jafari, R., Almqvist, H., Axelsson, H., Ignatushchenko, M., Lundback, T., Nordlund, P., and Martinez Molina, D. (2014) The cellular thermal shift assay for evaluating drug target interactions in cells. *Nat Protoc.* **9**, 2100-2122

44. Shaw, J., Dale, I., Hemsley, P., Leach, L., Dekki, N., Orme, J. P. *et al.* (2019) Positioning High-Throughput CETSA in Early Drug Discovery through Screening against B-Raf and PARP1. *SLAS Discov.* **24**, 121-132

45. Hengst, J. A., Dick, T. E., Smith, C. D., and Yun, J. K. (2020) Analysis of selective target engagement by small-molecule sphingosine kinase inhibitors using the Cellular Thermal Shift Assay (CETSA). *Cancer Biol Ther.* **21**, 841-852

46. Perrin, J., Werner, T., Kurzawa, N., Rutkowska, A., Childs, D. D., Kalxdorf, M. *et al.* (2020) Identifying drug targets in tissues and whole blood with thermal-shift profiling. *Nat Biotechnol.* **38**, 303-308

47. Van Vranken, J. G., Li, J., Mintseris, J., Gadzuk-Shea, M., Gygi, S. P., and Schweppe, D. K. (2024) Large-scale characterization of drug mechanism of action using proteome-wide thermal shift assays. *bioRxiv.*10.1101/2024.01.26.577428

48. Locke, T. M., Fields, R., Gizinski, H., Otto, G. M., Shechner, D. M., Berg, M. D. *et al.* (2024) High-Throughput Identification of Calcium Regulated Proteins Across Diverse Proteomes. *bioRxiv.*10.1101/2024.01.18.575273

49. Malinovska, L., Cappelletti, V., Kohler, D., Piazza, I., Tsai, T. H., Pepelnjak, M. *et al.* (2023) Proteome-wide structural changes measured with limited proteolysis-mass spectrometry: an advanced protocol for high-throughput applications. *Nat Protoc.* **18**, 659-682

50. Moggridge, S., Sorensen, P. H., Morin, G. B., and Hughes, C. S. (2018) Extending the Compatibility of the SP3 Paramagnetic Bead Processing Approach for Proteomics. *J Proteome Res.* **17**, 1730-1740

51. Hughes, C. S., Moggridge, S., Muller, T., Sorensen, P. H., Morin, G. B., and Krijgsveld, J. (2019) Single-pot, solid-phase-enhanced sample preparation for proteomics experiments. *Nat Protoc.* **14**, 68-85

52. Krieger, J. R., Wybenga-Groot, L. E., Tong, J., Bache, N., Tsao, M. S., and Moran, M. F. (2019) Evosep One Enables Robust Deep Proteome Coverage Using Tandem Mass Tags while Significantly Reducing Instrument Time. *J Proteome Res.* **18**, 2346-2353

53. Cox, J., and Mann, M. (2008) MaxQuant enables high peptide identification rates, individualized p.p.b.-range mass accuracies and proteome-wide protein quantification. *Nat Biotechnol.* **26**, 1367-1372

54. Elias, J. E., and Gygi, S. P. (2007) Target-decoy search strategy for increased confidence in large-scale protein identifications by mass spectrometry. *Nat Methods.* **4**, 207-214

55. Blum, B. C., and Emili, A. (2021) Omics Notebook: robust, reproducible and flexible automated multiomics exploratory analysis and reporting. *Bioinform Adv.*10.1093/bioadv/vbab024

56. Ritchie, M. E., Phipson, B., Wu, D., Hu, Y., Law, C. W., Shi, W., and Smyth, G. K. (2015) limma powers differential expression analyses for RNA-sequencing and microarray studies. *Nucleic Acids Res.* **43**, e47

57. Szklarczyk, D., Kirsch, R., Koutrouli, M., Nastou, K., Mehryary, F., Hachilif, R. *et al.* (2023) The STRING database in 2023: protein-protein association networks and functional enrichment analyses for any sequenced genome of interest. *Nucleic Acids Res.* **51**, D638-D646

58. Shen, L., and Pelletier, J. (2020) General and Target-Specific DExD/H RNA Helicases in Eukaryotic Translation Initiation. *Int J Mol Sci.* **21**, 4402

59. Calo, E., Flynn, R. A., Martin, L., Spitale, R. C., Chang, H. Y., and Wysocka, J. (2015) RNA helicase DDX21 coordinates transcription and ribosomal RNA processing. *Nature.* **518**, 249-253

60. Henn, A., Bradley, M. J., and De La Cruz, E. M. (2012) ATP utilization and RNA conformational rearrangement by DEAD-box proteins. *Annu Rev Biophys.* **41**, 247-267

61. Liu, F., Putnam, A. A., and Jankowsky, E. (2014) DEAD-box helicases form nucleotide-dependent, long-lived complexes with RNA. *Biochemistry.* **53**, 423-433

62. Li, J., Van Vranken, J. G., Paulo, J. A., Huttlin, E. L., and Gygi, S. P. (2020) Selection of Heating Temperatures Improves the Sensitivity of the Proteome Integral Solubility Alteration Assay. *J Proteome Res.* **19**, 2159-2166

63. Jarzab, A., Kurzawa, N., Hopf, T., Moerch, M., Zecha, J., Leijten, N. *et al.* (2020) Meltome atlas-thermal proteome stability across the tree of life. *Nat Methods.* **17**, 495-503

64. Lehman, S. L., Wechsler, T., Schwartz, K., Brown, L. E., Porco, J. A., Devine, W. G. *et al.* (2022) Inhibition of the Translation Initiation Factor eIF4A Enhances Tumor Cell Radiosensitivity. *Mol Cancer Ther.* **21**, 1406-1414

65. Zhang, X., Bi, C., Lu, T., Zhang, W., Yue, T., Wang, C. *et al.* (2020) Targeting translation initiation by synthetic rocaglates for treating MYC-driven lymphomas. *Leukemia.* **34**, 138-150

66. Pallett, M. A., Lu, Y., and Smith, G. L. (2022) DDX50 Is a Viral Restriction Factor That Enhances IRF3 Activation. *Viruses.* **14**, 316

67. Xu, K., Sun, S., Yan, M., Cui, J., Yang, Y., Li, W. *et al.* (2022) DDX5 and DDX17-multifaceted proteins in the regulation of tumorigenesis and tumor progression. *Front Oncol.* **12**, 943032

68. Gakh, O., Cavadini, P., and Isaya, G. (2002) Mitochondrial processing peptidases. *Biochim Biophys Acta.* **1592**, 63-77

69. Raimondi, M. V., Randazzo, O., La Franca, M., Barone, G., Vignoni, E., Rossi, D., and Collina, S. (2019) DHFR Inhibitors: Reading the Past for Discovering Novel Anticancer Agents. *Molecules.* **24**, 1140

70. Lomenick, B., Hao, R., Jonai, N., Chin, R. M., Aghajan, M., Warburton, S. *et al.* (2009) Target identification using drug affinity responsive target stability (DARTS). *Proc Natl Acad Sci U S A.* **106**, 21984-21989

71. Jeronimo, C., Forget, D., Bouchard, A., Li, Q., Chua, G., Poitras, C. *et al.* (2007) Systematic analysis of the protein interaction network for the human transcription machinery reveals the identity of the 7SK capping enzyme. *Mol Cell.* **27**, 262-274

72. Friesner, R. A., Banks, J. L., Murphy, R. B., Halgren, T. A., Klicic, J. J., Mainz, D. T. *et al.* (2004) Glide: a new approach for rapid, accurate docking and scoring. 1. Method and assessment of docking accuracy. *J Med Chem.* **47**, 1739-1749

73. Halgren, T. A., Murphy, R. B., Friesner, R. A., Beard, H. S., Frye, L. L., Pollard, W. T., and Banks, J. L. (2004) Glide: a new approach for rapid, accurate docking and scoring. 2. Enrichment factors in database screening. *J Med Chem.* **47**, 1750-1759

74. Sherman, W., Day, T., Jacobson, M. P., Friesner, R. A., and Farid, R. (2006) Novel procedure for modeling ligand/receptor induced fit effects. *J Med Chem.* **49**, 534-553

75. Gaudreault, F., Chartier, M., and Najmanovich, R. (2012) Side-chain rotamer changes upon ligand binding: common, crucial, correlate with entropy and rearrange hydrogen bonding. *Bioinformatics.* **28**, i423-i430

76. Chambers, J. M., Lindqvist, L. M., Savage, G. P., and Rizzacasa, M. A. (2016) Total synthesis of a biotinylated rocaglate: Selective targeting of the translation factors eIF4AI/II. *Bioorg Med Chem Lett.* **26**, 262-264

77. Chambers, J. M., Lindqvist, L. M., Webb, A., Huang, D. C., Savage, G. P., and Rizzacasa, M. A. (2013) Synthesis of biotinylated episilvestrol: highly selective targeting of the translation factors eIF4AI/II. *Org Lett.* **15**, 1406-1409

78. Van Vranken, J. G., Li, J., Mitchell, D. C., Navarrete-Perea, J., and Gygi, S. P. (2021) Assessing target engagement using proteome-wide solvent shift assays. *Elife.*10.7554/eLife.70784

79. Yu, Q., Liu, X., Keller, M. P., Navarrete-Perea, J., Zhang, T., Fu, S. *et al.* (2023) Sample multiplexing-based targeted pathway proteomics with real-time analytics reveals the impact of genetic variation on protein expression. *Nat Commun.* **14**, 555

80. Lacabanne, D., Wiegand, T., Wili, N., Kozlova, M. I., Cadalbert, R., Klose, D. *et al.* (2020) ATP Analogues for Structural Investigations: Case Studies of a DnaB Helicase and an ABC Transporter. *Molecules.* **25**, 5268

81. Bailey, M. A., Martyr, J. G., Hargrove, A. E., and Fitzgerald, M. C. (2024) Stability-Based Proteomics for Investigation of Structured RNA-Protein Interactions. *Anal Chem.* **96**, 3044-3053

82. Ditton, H. J., Zimmer, J., Kamp, C., Rajpert-De Meyts, E., and Vogt, P. H. (2004) The AZFa gene DBY (DDX3Y) is widely transcribed but the protein is limited to the male germ cells by translation control. *Hum Mol Genet.* **13**, 2333-2341

83. Xin, Y., and Zhang, Y. (2023) Paralog-based synthetic lethality: rationales and applications. *Front Oncol.* **13**, 1168143

84. Stegmann, K. M., Dickmanns, A., Gerber, S., Nikolova, V., Klemke, L., Manzini, V. *et al.* (2021) The folate antagonist methotrexate diminishes replication of the coronavirus SARS-CoV-2 and enhances the antiviral efficacy of remdesivir in cell culture models. *Virus Res.* **302**, 198469

85. Iaconis, D., Caccuri, F., Manelfi, C., Talarico, C., Bugatti, A., Filippini, F. *et al.* (2023) DHFR Inhibitors Display a Pleiotropic Anti-Viral Activity against SARS-CoV-2: Insights into the Mechanisms of Action. *Viruses.* **15**, 1128

86. Beck, S., Zhu, Z., Oliveira, M. F., Smith, D. M., Rich, J. N., Bernatchez, J. A., and Siqueira-Neto, J. L. (2019) Mechanism of Action of Methotrexate Against Zika Virus. *Viruses.* **11**, 338

87. Perez-Riverol, Y., Bai, J., Bandla, C., Garcia-Seisdedos, D., Hewapathirana, S., Kamatchinathan, S. *et al.* (2022) The PRIDE database resources in 2022: a hub for mass spectrometry-based proteomics evidences. *Nucleic Acids Res.* **50**, D543-D552